Title
Vision Changes the Cellular Composition of Binocular Circuitry during the Critical Period

Journal
Neuron, 108(4)

ISSN
0896-6273

Authors
Tan, Liming
Tring, Elaine
Ringach, Dario L
et al.

Publication Date
2020-11-01

DOI
10.1016/j.neuron.2020.09.022

Peer reviewed

HHS Public Access

Author manuscript

Neuron. Author manuscript; available in PMC 2021 November 25.

Published in final edited form as:

Neuron. 2020 November 25; 108(4): 735–747.e6. doi:10.1016/j.neuron.2020.09.022.

Vision changes the cellular composition of binocular circuitry during the critical period

Liming Tan[1,2], **Elaine Tring**[3], **Dario L. Ringach**[3,4], **S. Lawrence Zipursky**[1,2], **Joshua T. Trachtenberg**[3]

[1]Department of Biological Chemistry, David Geffen School of Medicine at UCLA, Los Angeles, CA 90095, USA.

[2]Howard Hughes Medical Institute.

[3]Department of Neurobiology, David Geffen School of Medicine at UCLA, Los Angeles, CA 90095, USA.

[4]Department of Psychology, University of California, Los Angeles, CA 90095, USA.

Summary:

High acuity stereopsis emerges during an early postnatal critical period when binocular neurons in the primary visual cortex sharpen their receptive field tuning properties. We find that this sharpening is achieved by dismantling the binocular circuit present at critical period onset and building it anew. Longitudinal imaging of receptive field tuning (e.g. orientation selectivity) of thousands of neurons reveals that most binocular neurons present in layer 2/3 at critical-period onset are poorly tuned and are rendered monocular. In parallel, new binocular neurons are established by conversion of well-tuned monocular neurons as they gain matched input from the other eye. These improvements in binocular tuning in layer 2/3 are not inherited from layer 4 but are driven by the experience-dependent sharpening of ipsilateral eye responses. Thus, vision builds a new and more sharply tuned binocular circuit in layer 2/3 by cellular exchange and not by refining the original circuit.

In Brief

Tan et al. demonstrate that visually evoked responses of binocular neurons improve across the critical period. This is caused by changing the cellular composition of the binocular pool. Poorly tuned binocular neurons become monocular while sharply tuned monocular neurons gain matched responses to the other eye and become binocular.

Lead Contact: Joshua Trachtenberg, joshua.trachtenberg@gmail.com.

Author Contributions:

Conceptualization, L.T., D.L.R., S.L.Z. and J.T.T.; Methodology, L.T. and E.T.; Investigation, L.T.; Software, D.L.R., and L.T.; Writing – Original Draft, L.T., D.L.R., S.L.Z. and J.T.T. Writing – Review & Editing, L.T., D.L.R., S.L.Z. and J.T.T; Funding Acquisition, D.L.R., S.L.R., and J.T.T.

Declaration of Interests: The authors declare no competing interests.

Data and Materials Availability: The databases and corresponding analysis and plotting codes are available upon request.

Introduction

Cortical circuitry in the mammalian brain is especially sensitive to and instructed by environment-specific stimuli (Espinosa and Stryker, 2012; Hooks and Chen, 2020; White and Fitzpatrick, 2007; WIESEL and HUBEL, 1963). The cortex is composed of many different neuron types and each of these forms a dense complex network of synaptic connections (Gouwens et al., 2019; Tasic et al., 2018). Early steps in the establishment of neural circuitry are governed by genetically hard-wired mechanisms mediated by cell recognition molecules, synaptic adhesion proteins, and sensory-independent neural activity (Ackman et al., 2012; Katz and Shatz, 1996; Ko et al., 2013, 2014; Sanes and Zipursky, 2020; Xu et al., 2011). This circuitry is then improved and solidified by experience, a stage in development referred to as the critical period (Espinosa and Stryker, 2012).

The impact of sensory experience on the development of cortical circuitry is perhaps best characterized in the primary visual cortex (Priebe and McGee, 2014). Visual information is processed within the retina and then transmitted by retinal ganglion cells to thalamocortical relay neurons. These neurons, in turn, project to the primary visual cortex forming synapses with layer 4 neurons and to a lesser extent with neurons in extragranular layers (Hooks and Chen, 2020; Kim et al., 2015; Niell, 2015). Within cortex, a complex translaminar and intralaminar web of feedforward and feedback synapses gives rise to feature detection not present at antecedent levels of visual processing (Priebe, 2016). This complexity requires the activity pattern of sensory receptors in the epithelium and is refined by experience (Ackman et al., 2012; Hoy and Niell, 2015; Paik and Ringach, 2011; Ringach, 2004).

The emergence of binocular neurons in cortex is especially sensitive to visual experience during a critical period of early postnatal development. In visual cortex, responses emerge first to contralateral eye stimulation (Crair et al., 1998; Smith and Trachtenberg, 2007). These responses, with the exception of direction tuning (Li et al., 2008; Smith et al., 2015), are innately established, are present at eye opening (Hoy and Niell, 2015; HUBEL and WIESEL, 1963; Ko et al., 2013), and continue to develop along their normal trajectory even in the absence of vision (Ko et al., 2014; Sherk and Stryker, 1976; White et al., 2001). Cortical responses to ipsilateral eye stimulation develop later and their development is regulated by vision (Crair et al., 1998; Faguet et al., 2009; Smith and Trachtenberg, 2007). A common view is that intrinsic mechanisms establish a rudimentary binocular circuitry that is subsequently improved by visual experience (Gu and Cang, 2016; Sarnaik et al., 2014; Wang et al., 2010, 2013). This is thought to involve gradual refinements in the orientation preferences of intrinsically established binocular neurons, enabling them to respond to the same features viewed by the two eyes (Espinosa and Stryker, 2012).

Here, we tracked the tuning properties of binocular and monocular neurons in layer 4 and 2/3 across the classically defined critical period in mouse visual cortex, which spans the fourth and fifth postnatal weeks (Gordon and Stryker, 1996). Our measures show that responses of layer 2/3 binocular neurons become significantly more selective to orientation, develop preferences to higher spatial frequency stimuli, and become more “complex”, or phase invariant. These improvements of feature selectivity do not occur by gradually

improving and matching receptive field tuning properties of existing binocular neurons. Instead, more than half of the binocular neurons present at critical period onset are poorly tuned for stimulus features and these neurons lose responsiveness to one eye and become monocular. In parallel, vision establishes new binocular neurons by conversion of the best tuned neurons drawn from the monocular contralateral pool. These well-tuned monocular neurons gain matched responses from the ipsilateral eye. We demonstrate that this transformation of the binocular circuit requires vision-dependent maturation of cortical responses to the ipsilateral eye, is not driven by changes in layer 4 and is unique to the critical period. Together, these findings show that binocular feature selectivity improves across the critical period and define mechanisms by which vision drives this process.

RESULTS

Receptive field tuning measured from GCaMP6s responses

To obtain a clearer view of the development of binocularity in primary visual cortex, we measured receptive field tuning of pyramidal neurons expressing the genetically encoded calcium indicator GCaMP6s (Chen et al., 2013) in critical period (P22-P36) and adult (>P56) mice (Gordon and Stryker, 1996). For each mouse used in this study, the binocular zone was identified as the overlap of contralateral and ipsilateral eye visual field sign maps obtained from epifluorescence retinotopic mapping of GCaMP6s responses (Figure 1A; Garrett et al., 2014; Kalatsky and Stryker, 2003; Wekselblatt et al., 2016). This map was used to target subsequent high magnification, cellular resolution, resonant scanning 2-photon imaging of GCaMP6s signals (Figure 1B, C). During 2-photon imaging, mice were head-fixed but otherwise alert and free to walk on a cylindrical treadmill. Receptive field tuning for each imaged neuron was estimated from the linear regression of the temporally deconvolved calcium response (Figure 1D) to a sequence of flashed, high-contrast sinusoidal gratings of 18 orientations and 12 spatial frequencies presented at 8 spatial phases for each combination of orientation and spatial frequency (Mineault et al., 2016; Methods). For each imaged cell, a “kernel” plotting response strength across orientations and spatial frequencies was obtained. An example of one such kernel and its emergence as a function of time after stimulus onset is given in Figure 1E (an example of a visually unresponsive neuron is given in Figure S1A,B). Receptive field tuning kernels whose signals were significantly higher than noise were recovered from approximately 70% of imaged neurons (Figure 1F; see also Methods and Figure S2 for methodological details). This value is in close agreement with electrophysiological measures made from head-restrained, alert mice where 60%-80% of neurons are found to be visually responsive (Hoy and Niell, 2015). Binocular neurons were those in which tuning kernels could be measured in response to separate stimulation of each eye. A qualitative comparison of SNR and receptive field tuning kernels is given in Figure S3.

For each neuron, three measures of receptive field tuning were made: 1) orientation selectivity, 2) spatial frequency preference, and 3) complexity. Orientation selectivity was measured as circular variance (see Methods and Figure S1C). Cells that are highly selective, and thus respond to a very narrow range of orientations have lower circular variance. Spatial frequency preference is a measure of spiking as a function of the spacing between lines of

the grating. Complexity was measured as the F1/F0 ratio (Skottun et al., 1991; see Methods). So-called “simple” cells respond optimally when a stimulus of a particular orientation and spatial frequency falls within a specific region of that cell’s receptive field. Complex cells, by contrast, are phase-invariant; their responses are unaffected by positional variations of the stimulus within the receptive field (Hubel and Wiesel, 1962, 1968; Ohzawa et al., 1997a; Skottun et al., 1991). Lower F1/F0 values indicate greater complexity and, thus, greater phase invariance. For binocular neurons, a fourth measure was taken: binocular matching. This is a measure of similarity between tuning responses measured through each eye separately. This was calculated as the correlation coefficient of the tuning kernels obtained from each eye (Jimenez et al., 2018). Neurons with similar tuning have higher matching coefficients.

Turnover between binocular and monocular cell groups

To examine the development of binocular neurons in layer 2/3 across the critical period, we made repeated measures of receptive field tuning from the same cells at P22, P29, and P36 (1,064 neurons in four mice tracked across these three time points; Figure 2A; see also Methods and Figure S4 and S5). These measures revealed that the cellular composition of the binocular pool changed across the critical period; cells that were binocular at one time point were often monocular at subsequent time points and vice-versa. Of 160 neurons that were binocular at P22, only 64 (40%) remained binocular at P29. This conversion of binocular neurons to monocular was offset by the conversion of a different group of monocular neurons to binocular; 128 previously monocular or non-responsive neurons became binocular, resulting in a 20% increase in the size of the binocular pool from 160 to 192 neurons. This pattern of loss and replenishment continued into the fifth postnatal week (P29 to 36), though consistent with a tapering of plasticity as the critical period wanes, these dynamics slowed. From P29 to P36, 86 binocular cells were lost, and 91 new binocular neurons were gained. The number of binocular neurons created by the addition of ipsilateral eye inputs to previously contralateral, monocular neurons was 2.4 times larger than the number created from initially ipsilateral monocular cells gaining contralateral responsiveness (138 vs 57). Examples of ipsilateral and contralateral eye tuning kernels of functionally stable neurons, of neurons that became monocular and neurons that became binocular are shown in Figure 2B-D, respectively.

As a further validation of our approach to identifying the same cells at each time point (see also Methods and Figure S6), we examined the similarity of the receptive field tuning kernels of each tracked cell across the three time points. We reasoned that if the same neuron is tracked, its tuning preferences should remain fairly stable. This similarity from one time point to the next can be measured as the correlation coefficient of the tuning kernels obtained at each time point. For monocular neurons, coefficients are obtained by comparing a given neuron’s tuning kernel measured on P22 to that measure on P29, and then again between P29 and P36. For binocular neurons that become monocular, the tuning kernel for one of the eyes can be measured before and after this transition across all 3 time points. The same is true for cells that were monocular and became binocular. In mice, contralateral eye responses are dominant. We, therefore, examined the matching coefficients of contralateral eye responses of tracked cells and compared the distributions of these coefficients to the

distribution of coefficients obtained when tuning kernels were randomly matched, as would occur if different cells were inadvertently tracked at each time point. In all cases, the distributions of matching coefficients could not occur by chance (Figure 2E). To illustrate this more clearly, we plot examples of receptive field tuning kernels with coefficients from 0.08 to 0.97 in Figure 2F. Kernels with matching coefficients above 0.5 are qualitatively well matched. Using this as a benchmark, 93% percent (790/854) of stable monocular neurons, 89% (75/84) of binocular neurons that became monocular contralateral, and 93% (128/138) of monocular, contralateral neurons that became binocular had matching coefficients greater than 0.5 (Figure 2E).

These data indicate that the pool of binocular neurons at critical period closure is different from the pool at critical period onset. Most binocular neurons present at the beginning of the critical period are rendered monocular or unresponsive while many previously monocular neurons gain input from the other eye and become binocular as the critical period progresses.

Stable and newly formed binocular neurons have highly selective receptive field tuning

We wondered whether receptive field tuning had an influence on which neurons became binocular or monocular. We found that binocular neurons with sharper orientation selectivity, higher spatial frequency preferences, and greater complexity had high binocular matching coefficients. These were significantly more likely to remain binocular than binocular neurons with poorer selectivity, reduced complexity, and poorer matching (Figure 3A-D). In most cases, the strongest input was maintained as the weaker was lost (Figure 3E), and this loss was due to a large drop in SNR of approximately 4-times the standard deviation of noise mean (Figure 3F). Simply put, binocular neurons that were sharply tuned, driven by higher spatial frequency stimuli, and of greater complexity were maintained. Those that were broadly tuned and responded to lower spatial frequency stimuli ultimately lost responsiveness to the weaker eye and became monocular (Figure 3G).

A similar analysis of monocular neurons that gained responsiveness to the other eye and thus became binocular neurons showed that these neurons were better tuned than monocular neurons that remained monocular (Figure 4A-C; Figure S7 plots tuning measures for each mouse). Moreover, ipsilateral and contralateral eye tuning kernels were better matched in newly formed binocular neurons than they were in binocular cells that became monocular (Figure 4C). We did not see the gradual matching of ipsilateral and contralateral eye orientation preferences proposed by existing models. For those neurons that gained responsiveness to an eye, the tuning kernels experienced a large increase in SNR relative to the previous imaging session, and these increases were significantly larger than any SNR changes measured in otherwise stable tuning kernels (Figure 4D; see also Figures S8-9). Thus, here as well, a neuron’s fate was determined by its receptive field tuning properties; monocular neurons with broad tuning remained monocular while those with sharp tuning and higher spatial frequency preferences gained matched input from the other eye and were converted to binocular neurons (Figure 4E).

Together, the data in Figures 3 and 4 indicate that sharply tuned binocular neurons that were established prior to the critical period are maintained while those poorly tuned binocular

neurons lose responsiveness to one eye and are jettisoned to the monocular pool. In parallel, the size of the binocular pool is maintained (and increased somewhat) by converting the best-tuned monocular neurons into binocular neurons. In this manner, the tuning of the binocular pool improves across the critical period at the expense of the monocular pool. When we expanded our view to include all cells imaged at P22, P29, and P36 (not only longitudinally tracked neurons), it was evident that the progressive improvement of binocular responses occurred in lock step with, and was likely caused by the progressive improvement of ipsilateral eye responses (Figure S10).

We next set out to ask whether this exchange of neurons and the improvement in their tuning properties required vision, was unique to layer 2/3, and was temporally restricted to the critical period.

Recruitment but not elimination requires vision

To assess the role of vision in this process we measured receptive field tuning and binocular matching in mice that were normally reared until P22 and then placed in the dark from P22 through P36. These mice were imaged prior to dark exposure at P22, again at P29 while they viewed for two hours the high-contrast sinusoidal gratings before returning to darkness, and again at P36. This near complete absence of vision reduced the normal exchange of neurons between the binocular and monocular pools (three mice, 560 neurons longitudinally tracked). Without vision, receptive field tuning properties of monocular neurons that gained responsiveness to the other eye and became binocular were no better tuned than those that remained monocular, and these newly formed binocular neurons were simpler than monocular neurons that remained monocular (Figure 5A). Thus, vision plays a key role in converting monocular neurons with complex receptive fields, strong orientation selectivity, and higher spatial frequency preferences into binocular neurons.

The loss of binocular neurons, however, followed the same pattern as we observed in normally sighted mice. Binocular neurons that became monocular in the absence of vision had broader orientation selectivity, responded to lower spatial frequencies and were more poorly matched than stable binocular neurons (Figure 5B). As in normally sighted mice, the stability of binocular neurons (i.e. their lifetimes) was correlated with circular variance (Figure 5C); neurons with the sharpest tuning were most stable. Figure S11 plots receptive field tuning measures for each mouse separately.

Ipsilateral eye tuning did not improve in the absence of vision. Vision, however, does not appear to strongly influence contralateral eye tuning (Figure 5D). This immature ipsilateral eye tuning may limit the selectivity and matching of binocular neurons and this limitation could explain why binocular tuning fails to improve in the absence of vision (see Discussion).

No improvement in L2/3 in older mice

To determine if the turnover of the binocular pool and improvements of binocular tuning in layer 2/3 are restricted to the critical period, we took repeated weekly measures of receptive field tuning in three mice that were each older than P56 (Figure 6A), which is well past the closure of the critical period in mice. We first looked at the tuning distributions of all cells

imaged at each time point. No improvement of binocular or monocular neurons was found across either one- or two-week time intervals (Figure S12). Measures of 450 longitudinally tracked cells showed that the degree of turnover was also less in adults (32%, Figure 6B) and, correspondingly, the fraction of stable neurons was higher (62%, 56/91) compared to the critical period (22%, 44/197, p = 8.21e-11, Chi-square test). Moreover, cells that joined the binocular pool were not better tuned than those that became monocular (Figure 6C). These data show that the turnover of binocular neurons is markedly reduced in the adult and, by contrast to the critical period, there was no improvement in the tuning of binocular neurons.

No improvement in the layer 4 binocular ensemble

The conventional view of cortical development is that changes in layer 2/3 reflect and amplify changes that occur in the thalamorecipient layer 4 (Freeman and Olson, 1982; Shatz and Stryker, 1978). We therefore checked whether the improvements of binocular tuning that we observed in layer 2/3 are also found in layer 4. Measures of receptive field tuning were made at P22, P29, and P36 in mice in which GCaMP6s expression was restricted to layer 4 (717 neurons longitudinally imaged in 4 mice, Figure 7A). The turnover of binocular neurons in layer 4 was similar to that in layer 2/3. Of the 717 neurons tracked across the critical period, 155 were binocular at P22. Fifty-seven of these (37%) remained binocular at P29 while 75 new binocular neurons were established, resulting in a net reduction in the size of the binocular pool. From P29 to P36, 86 binocular neurons were lost as 39 were gained, again resulting a net contraction of the binocular pool. In contrast to layer 2/3, neither receptive field tuning, nor complexity, nor binocular matching improved in layer 4 binocular neurons (Figure 7B,C; Figure S13). Moreover, all of these measures of receptive field tuning from layer 4 were worse than measures from layer 2/3. Lastly, and again in contrast to layer 2/3, we found no improvement in ipsilateral eye tuning in layer 4 across the critical period (Figure 7D). These data indicate that the improvements in layer 2/3 binocular tuning are not inherited from layer 4.

Discussion

Binocular vision begins to emerge shortly after birth and is actively refined during a critical period of visual cortical development. In humans, this begins about 2-4 months after birth and continues through the first years of infancy and early childhood (Fawcett et al., 2005). In mice, this begins approximately 3 weeks after birth and is complete by the sixth postnatal week (Gordon and Stryker, 1996). Binocular vision is grounded in the establishment of binocular neurons in primary visual cortex (Ohzawa et al., 1997b). In contrast to the conclusion drawn from earlier studies (Wang et al., 2010; Xu et al., 2020), we show that the feature selectivity (e.g. orientation, spatial frequency, and complexity) of binocular neurons improves during the critical period and this is achieved by exchanging neurons between monocular and binocular pools based on their receptive field tuning. Moreover, we show that visual experience drives this process as it progressively improves ipsilateral eye receptive field tuning. We find no evidence for a progressive matching of initially unmatched orientation tuning (Wang et al., 2010; Xu et al., 2020).

Receptive field tuning of contralateral eye responses is fully mature at critical period onset, representing a full range of complexity, orientation and spatial frequency tuning. Ipsilateral eye tuning, by contrast is initially poor at critical period onset and feature selectivity significantly improves only with normal vision. As a result, binocular neurons are initially poorly selective for visual features. Three processes then re-make the population of binocular neurons during the critical period. First, the majority of binocular neurons prior to the critical period (>60%) are poorly tuned and rendered monocular. Second, binocular neurons that were well-tuned are retained. Retention is more efficient with vision. And finally, as ipsilateral eye responses sharpen with vision, they establish connections with similarly well-tuned contralateral monocular neurons and these become binocular. A schematic overview is given in Figure 8.

A parsimonious model for the emergence of sharper binocular tuning in layer 2/3 is that the improvement in ipsilateral eye responses during the critical period drives the improvement of binocular tuning. Monocular neurons that gain input from the other eye will only maintain this new input if it matches the host; postsynaptic responses driven by each eye will be coincident and thus both will be maintained in models of timing-dependent synaptic plasticity (Bi and Poo, 1998; Debanne et al., 1998; Feldman, 2012; Markram et al., 1997; Song et al., 2000). In the case of tuning mismatch, the weaker eye's input is lost. In this manner, feature selectivity of the binocular pool improves with normal vision as better tuned monocular neurons are recruited to the binocular pool as ipsilateral eye tuning improves.

The exchange of neurons between monocular and binocular pools also occurs in layer 4, but the tuning properties of layer 4 binocular neurons do not improve across the critical period. In this layer, as well, binocular tuning is limited by the tuning of the ipsilateral eye. Receptive field tuning of contralateral eye responses in layer 4 and 2/3 are indistinguishable. It is only the tuning of ipsilateral eye responses that differs between the two layers. Notably, ipsilateral eye tuning in layer 4 does not improve with vision across the critical period. Vision only appears to improve this tuning in layer 2/3, lending support to the model in which plasticity in layer 2/3 is driven by progressive improvements in ipsilateral eye tuning and are not inherited from layer 4 (Liu et al., 2008; Trachtenberg et al., 2000).

Somatostatin-expressing inhibitory neurons (SST cells) in layer 2/3 are well positioned to drive this sharpening of feature selectivity. These neurons are centrally involved in synaptic plasticity as they control dendritic spiking and synaptic integration as well as top-down modulation (Urban-Ciecko and Barth, 2016; van Versendaal and Levelt, 2016; Yavorska and Wehr, 2016). Their responses mature during the critical period (Lazarus et al., 2011) and the inhibition provided by SST cells sharpens orientation tuning selectivity and feature coding of pyramidal neurons (Adesnik et al., 2012; Wilson et al., 2012). Moreover, suppressing SST cell activity during the critical period impairs the maturation of ipsilateral eye responses and the emergence of binocularity in layer 2/3 (Yaeger et al., 2019). This suggests a broader view of inhibition during the critical period with fast spiking basket cells inhibiting somatic spiking (van Versendaal and Levelt, 2016) and SST neurons regulating dendritic responses acting together to promote the emergence of stable binocular neurons.

In conclusion, the studies we report here indicate that vision, and perhaps sensory experience more generally in other regions of the cortex, constructs new functional ensembles during the critical period rather than refining the ensemble in place at critical period onset. This appears to be achieved by exploiting a heightened instability unique to this period of development. Defining the sources of this instability, the targets of experience at the cellular and molecular levels, and the means by which experience integrates one set of inputs into an otherwise hard-wired circuitry are crucial questions for future studies.

STAR Methods

RESOURCE AVAILABILITY

Lead Contact—Further information and requests for resources and reagents should be directed to and will be fulfilled by the Lead Contact, Joshua Trachtenberg (joshua.trachtenberg@gmail.com).

Materials Availability—This study did not generate new unique reagents.

Data and Code Availability—Custom-written MATLAB code and data for this study are available from the Lead Contact upon request.

EXPERIMENTAL MODEL AND SUBJECT DETAILS

All procedures were approved by UCLA's Office of Animal Research Oversight (the Institutional Animal Care and Use Committee, IACUC) and were in accord with guidelines set by the US National Institutes of Health. Normally reared mice were housed in groups of 2-3 per cage in a normal 12/12 light dark cycle. Dark-reared mice were housed in groups of 1-3 per cage in a light-tight cabinet that was additionally shielded with two layers of polyurethane-coated black nylon sheet (Thorlabs, BK5). Animals were naïve subjects with no prior history of participation in research studies. A total of 19 mice, both male (11) and female (8) were used in this study (Critical period layer 2/3 normally reared, 4 males; Critical period layer 2/3 dark reared, 2 males and 1 female; adult layer 2/3, 3 females; critical period layer 4 normally reared, 2 males and 2 females; imaging focal plane displacement, 3 males and 2 females).

Mice: All imaging was performed on mice expressing the slow variant of GCaMP6 in pyramidal neurons. For layer 2/3 imaging, these mice were derived from crosses of B6;DBA-Tg(tetO-GCaMP6s)2Niell/J (JAX Stock No: 024742; Wekselblatt et al., 2016) with B6;CBA-Tg(Camk2a-tTA)1Mmay/J (JAX Stock No: 003010; Mayford et al., 1996). For layer 4 imaging, these mice were derived from crosses of B6;C3-Tg(Scnn1a-cre)3Aibs/J (JAX Stock No: 009613) (Madisen et al., 2010) with Ai163 (Daigle et al., 2018) (Gift from Dr. Hongkui Zeng in Allen Institute). Mice expressing both transgenes were identified by PCR, outsourced to Transnetyx (transnetyx.com).

METHODS DETAILS

Surgery—All epifluorescence and two-photon imaging experiments were performed through chronically-implanted cranial windows as in Yaeger et al., 2019. In brief, for critical

period experiments, mice at P14-P16 were administered with carprofen analgesia prior to surgery. Mice were anesthetized with isoflurane (5% for induction; 1.5–2% during surgery); body temperature was maintained at 37°C. A thin layer of ophthalmic ointment was applied to both eyes to prevent desiccation. Anesthetized mice were mounted on a stereotaxic surgical stage and the head secured by ear bars and a mouth bar. Scalp overlying the parietal plates on both hemispheres of the skull was removed. After the exposed skull dried, it was covered by a thin layer of Vetbond at the junction of any muscle or skin; this junction was further sealed by a layer of black dental acrylic. A stainless-steel head bar was affixed with dental acrylic caudally to V1. Note the headbar needs to be leveled and parallel to a virtual line connecting the two eyes. A high-speed dental drill was used to remove a 3.5 mm diameter portion of the exposed skull overlying V1 on the left hemisphere; care was taken not to damage the dura. A sterile 3 mm diameter cover glass was place inside the craniotomy to cover the exposed brain and then sealed to the surrounding skull with Vetbond. The edges, as well as the remainder of the exposed skull and surgery margins were sealed with dental acrylic. Mice were recovered on a water-circulating heating pad. When alert, they were placed back in their home cage. Carprofen was administered daily for 3 days post-surgery. Mice were left to recover for 4-7 days prior to imaging. For adult experiments (imaging started at P56, P60 and P77 for each mouse, respectively), surgeries were performed 10-14 days before experiments. For experiments on imaging effects of focal plane displacement (Figure S5), we performed surgery on 5 mice at P18, P19, P27, P37 and P48, respectively.

Mapping of binocular area of the primary visual cortex—The binocular region of primary visual cortex on the left hemisphere for each mouse used in this study was identified using low magnification, epifluorescence imaging of visually-evoked GCaMP6s signals (Salinas et al., 2017; Wekselblatt et al., 2016). GCaMP6s was excited using a 470nm light-emitting diode. The monitor was positioned relative to each mouse so that the binocular field fell in the middle of the monitor. To map azimuth and elevation we followed a procedure adapted from Kalatsky and Stryker, 2003. We presented a contrast reversing checkerboard (checker size 4x4 deg) windowed by a 1D Gaussian along the horizontal or vertical axis. The Gaussian envelope drifted normal to its orientation to complete a sweep of the entire screen in 10 sec. We used both directions of motion to estimate neural delay and obtain an absolute phase map. The screen size was 120 deg in azimuth and 80 deg in elevation and the monitor was placed 19 cm from the eyes. Eight cycles were recorded for each of the four cardinal directions. Images of GCaMP6s-mediated fluorescent changes were acquired through the camera path of the two-photon microscope (Neurolabware, Los Angeles, CA) equipped with a PCO edge 4.2 m HQ sCMOS camera using a 4X microscope objective (Olympus, 0.16 numerical aperture). Images were acquired at 10 or 15 frames per second. The camera was focused approximately 100 μm below the pia surface. Visual stimulus presentation and image acquisition were controlled by custom written software in Processing sketch using OpenGL shaders (see https://processing.org) and Matlab (Mathworks). Transistor-transistor logic signals generated by the stimulus computer were sampled by the microscope and time-stamped with the frame imaged at that time. This provided the synchronization between visual stimulation and imaging data. Retinotopic maps of azimuth and elevation were generated from these images as in Kalatsky and Stryker, 2003, and visual field sign maps were calculated as in Garrett et al., 2014. The binocular area of the primary

cortex was defined as the region of primary visual cortex driven by both the contralateral and ipsilateral eyes (Figure 1A).

Two photon calcium imaging—2-photon imaging was targeted to the binocular zone of V1 based on the epifluorescence mapping described above. Imaging was achieved using a resonant/galvo scanning two-photon microscope (Neurolabware, Los Angeles, CA) controlled by Scanbox image acquisition software (Los Angeles, CA). GCaMP6s was excited by a Coherent Discovery TPC laser (Santa Clara, CA) running at 920 nm focused through a 16x water-immersion objective lens (Nikon, 0.8 numerical aperture). The objective was set at an angle of 10 to 15 degrees from the plumb line during imaging to reduce the slope of the imaging planes relative to the pia surface. Image sequences (512x796 pixels, 490x630 μm) were captured at 15.5 Hz at a depth of 90 to 320μm below the pial surface for layer 2/3 imaging, and 350 to 500μm below pia surface for layer 4 imaging. All imaging was performed on alert, head-fixed mice that were free to move on a 3D-printed running wheel. A rotary encoder placed with its post through the wheel axel was used to record running. Eye movements and fluctuations in pupil diameter were recorded using a Dalsa Genie M1280 camera (Teledyne Dalsa) fitted with a 740nm long-pass filter to image infrared laser light scattered through the brain and out the pupil. Both the rotary encoder and eye tracking cameras were triggered at scanning frame rate. To measure response properties of neurons to each eye separately, an opaque patch was placed immediately in front of one eye when recording the responses of neurons to visual stimuli presented to the other eye.

Visual stimulation during 2-photon imaging—Prior to acquiring data sets, the retinotopic position of the imaging field of view (FOV) was mapped using a series of small, flashing checkerboard squares to evoke responses. Based on these measures, the position of the monitor was adjusted so that the receptive fields within the imaging FOV were located on the center of the screen. The monitor size was 27 inch, was placed ~20 cm from the eyes, and covered ~112 degrees in azimuth and ~64 degrees in elevation. Stimulus contrast was set at 80%.

Flashing sinusoidal gratings: Visual stimulation for measuring response properties of neurons were the same as in Jimenez et al., 2018. Briefly, a set of sinusoidal gratings with different orientation, spatial frequency and spatial phase were generated in real-time by a Processing sketch using OpenGL shaders (see https://processing.org). The orientation domain was sampled at equal intervals of 10 degrees from 0 to 170 degrees; the spatial frequency domain was sampled in 12 equal steps on a logarithmic scale from 0.0079 to 0.1549 cycles per degree. For each combination of orientation and spatial frequency, spatial phase was equally sampled at an interval of 45 degrees from 0 to 315 degrees. Static gratings with different combinations of orientation, spatial frequency and spatial phase were presented at a rate of 4 Hz in pseudo-random sequence on a screen refreshed at 60 Hz. Imaging sessions were 15 min long (3600 stimuli in total), so each combination of orientation and spatial frequency appeared 16 or 17 times, and each spatial phase for an orientation/spatial frequency combination appeared twice (responses of neurons as a function of spatial phase is used to calculate F1/F0 values). To synchronize visual stimulation and imaging data, transistor-transistor logic signals generated by the stimulus

computer were sampled by the microscope and time-stamped with the frame and line number being scanned at that time.

Analysis of two-photon imaging data

Image processing: The pipeline for image processing is described in Ringach et al., 2016, with modifications for processing imaging planes consisting of cells whose visual responses were recorded to two eyes separately. Briefly, movies from the same plane for each eye were concatenated to a single file. Images in this file were aligned to correct for frameshift caused by motion during imaging (Figure S3A). The mean image of each plane generated after alignment was used to find the same cells for longitudinal imaging. For segmentation of pyramidal neurons, a Matlab graphical user interface tool (Scanbox, Los Angeles, CA) was used to define regions of interest (ROI) corresponding to cell bodies. This segmentation tool was first set to collect 600 to 1200 evenly spaced frames from the motion-corrected movie. This represents ~2-4% of all imaging frames per experiment. These frames were used to calculate pixel-wise correlations of fluorescence changes over time. The upper limit on the number of frames used to calculate this correlation map was determined by GPU performance (Nvidia Quadro M5000). The temporal correlation of pixels was used to define the boundaries of each neuron (Figure S3B) (Ringach et al., 2016). After segmentation, the fluorescence signal for each cell was extracted by computing the mean of the calcium fluorescence within each ROI and subtracting the median fluorescence from the nearby neuropils (Figure S3C,D) (Ringach et al., 2016). Neural spiking was then estimated via non-negative temporal deconvolution of the extracted signal using Vanilla algorithm (Berens et al., 2018). Non-negative deconvolution outperforms supervised algorithms (Pachitariu et al., 2018). After signal extraction and deconvolution, fluorescent signals and estimated spikes for each cell were split into separate files, corresponding to the separate imaging sessions for the two eyes. In this way, a single index was assigned to each cell, whose responses to each eye were calculated separately, to measure receptive field tuning properties and to define cells as binocular, contralateral monocular, ipsilateral monocular, or visually unresponsive. Each imaging experiment was independently segmented. Segmentation also gave rise to a mask file (796x512 matrix) in which ROIs were labeled by their index numbers; these were used to track the same cells imaged across days (Figure S3B).

Calculation of response properties

Signal to noise ratio (SNR) of visual response and identification of visually responsive neurons: SNR was used to identify neurons with significant visual responses. First, reverse correlation (Jimenez et al., 2018; Ringach et al., 1997, 2016) of spiking estimation relative to stimulus onset was used to locate the optimal delay for preferred stimuli (Figure 1E). The optimal delay is the frame at which the spiking standard deviation reached its maximum, which indicates the timing of each cell's peak responses as a function of stimulus onset. This occurred five to seven frames after stimulus onset. SNR for each neuron was calculated based on this timing, with signal being the mean of spiking standard deviation at 5-7 frames after stimulus onset, and noise as this value at frames well before or after stimulus onset (frames −2 to 0, and 13 to 17). Second, this measure of SNR as well as optimal delay were used to score cells as visually responsive or unresponsive. Optimal delay as a function of SNR is plotted for all cells imaged in this study (Figure S2A). Neurons whose optimal

delays occurred outside of the time-locked stimulus response window of 4 to 8 frames (padded by ±1 frame around the 5-7 frame range used above; Figure S2A, blue highlight) were spontaneously active, but otherwise visually unresponsive (see Figure S1A,B for example of a visually unresponsive neuron). They had low SNR values (close to 1) and their optimal delays were not time locked to any stimulus. The SNR values of these unresponsive neurons were normally distributed (mean = 1.0) over a narrow range (Figure S2B, blue shaded histogram). Since spontaneously active but otherwise visually unresponsive neurons could have optimal delays at any imaging frame relative to stimulus onset, some will naturally occur in the 4-8 frame time window when visually driven responses also occur (Figure S2B, red shaded). These can be distinguished from visually responsive neurons by SNR. This threshold is defined by the distribution of SNR values obtained above from the spontaneously active neurons. As a conservative measure we set this threshold at 3 standard deviations above the mean SNR of the normal distribution (Figure S2B, vertical black line). Notably, the outcome is independent of SNR threshold (Figure S8) and nor does it depend on the binarization of responses into monocular or binocular bins (Figure S9). Visually responsive neurons had optimal delays between frames 4 and 8, and SNRs greater than this cutoff. The fraction of visually responsive neurons obtained with this approach matches that obtained with electrophysiology measures of neural spiking in alert mice (Hoy and Niell, 2015). SNR values were calculated separately for responses to the ipsilateral or contralateral eye (Figure S1C). These plots for all cells imaged at P22, P29 and P36 are given in Figure S2C-H; note the similarity across ages.

F1/F0 measurement for phase-invariance: The modulation ratio, F1/F0, was used to measure phase invariance of each neuron's response. The sinusoidal visual stimulus gratings used in this study were presented at different spatial phases (Ringach et al., 2002). F1/F0 is the ratio of the amplitude of the post-stimulus time histogram (F1, 1^{st} Fourier harmonic) for a given cell and its mean firing rate (F0, 0^{th} Fourier harmonic). For complex cells the amplitude of F1 is smaller than F0 (F1/F0 < 1), while for simple cells this relationship is inverted (F1/F0 > 1) (Skottun et al., 1991).

Tuning kernel for orientation and spatial frequency: The estimation of the tuning kernel was performed as in earlier studies by fitting a linear model between the response and the stimulus (Ringach et al., 2016). Cross-correlation maps were used to assess each neuron's spiking level to each visual stimulus (orientation and spatial frequency) (Figure 1E). Cross-correlation maps were computed by averaging responses over spatial phases. The final tuning kernel of a neuron was defined as the correlation map at the optimal delay (Figure 1E, frame 6). Orientation and spatial frequency preference, circular variance and binocular matching coefficient were all calculated using tuning kernels for neurons whose SNR exceeded the noise threshold. Example kernels are given in Figure S1C.

Orientation and spatial frequency preference: Orientation and spatial frequency preferences were calculated using horizontal (for spatial frequency) and vertical (for orientation) slices of the tuning kernel passed through the peak response. That is, for any given cell, the slice for orientation is a 1x18 array, O_n, in which a level of estimated spiking (O_1 to O_{18}) occurs at orientations θ_n (0 to 170 degrees, spaced every 10 degrees). Similarly,

the slice for spatial frequency is a 1x12 array, Sfk, in which a level of estimated spiking (Sf_1 to Sf_{12}) occurs at spatial frequencies ω_k (12 equal steps on a logarithmic scale from 0.0079 to 0.1549 cycles per degree). Preferred orientation and spatial frequency were computed as the center of mass of the slices as:

$$orientation = \frac{\arctan(\sum_n O_n * e^{i*2*\pi*\theta_n / 180})}{2}$$

Orientation calculated in this formula is in radian, and was further converted to degrees.

$$spatial\,frequency = 10^{\frac{\sum_k Sf_k * \log_{10}\omega_k}{\sum_k Sf_k}}.$$

Circular variance: The circular variance, cv, of a neuron with estimated spiking of O_n at orientations θ_n (0° to 170°, spaced every 10°), is defined by

$$cv = 1 - \left| \frac{\sum_n O_n * e^{i*2*\pi*\theta_n / 180}}{\sum_n O_n} \right| . \quad (3)$$

Circular variance is a measure of orientation selectivity, with limits at zero and one. Neurons that do not have orientation tuning have a circular variance of 1. Neurons that are highly orientation selective have circular variance values close to 0 (see examples in Figure S1C).

Binocular matching coefficient: The matching coefficient for binocular neurons was defined as the correlation coefficient between their contralateral and ipsilateral tuning kernels.

Longitudinal imaging: The same imaging plane was located across days using images acquired on previous imaging days as reference. These include the vascular map at the pia acquired through the PCO camera and the mean motion-corrected fluorescence images of the two photon imaging experiments. Depth of each imaging plane from the pial surface was also written down to facilitate same imaging plane identification. Care was taken to ensure that the mount used to affix each mouse under the microscope objective lens was unchanged in angle or position. During subsequent imaging sessions, using the same objective angle as previous sessions, the approximate region for each imaging plane was first found by matching the imaging region with the corresponding vascular map reference and depth from pia. Fine adjustment of imaging depth was made by manual z-scanning in small steps of 2 μm for ~20 μm while running visual stimulation to identify the imaging plane that matched the mean image of the same plane acquired previously. For layer 4 imaging, the tdTomato image for each plane was also used to match imaging planes. Imaging planes were considered to be near identical when the position and diameter of the radial vasculature patterns matched, when cell morphology across the four quadrants of the image matched, and when the spatial clustering of local groups of cells across the image matched. An

examination of the impact of small variations in focal plane on receptive field tuning and binocularity is given below.

Finding longitudinally imaged cells: During segmentation, a single index number was assigned to each segmented neuron. Since segmentation was performed independently to experiments acquired on different days, the same neurons tracked often had different index numbers across days. Thus, finding the same cells imaged across multiple days involved matching the index numbers for experiments on different days for tracked neurons. This was achieved by assembling an index matrix for cells tracked across multiple days. To identify neurons tracked between adjacent days, a control point-based affine geometric transformation (Matlab syntax: cpselect, fitgeotrans and imwarp) was performed to correct the plane rotation (Figure S4A-C). This transformation was applied to the mask of the cells imaged on the second time point. The overlap of ROIs between the mask file from the first imaging time point and transformed mask file from the second imaging time point was calculated. If the overlapping area between two ROIs A and B was bigger than 50% of the union area of A and B ($A \cap B > 0.5*(AUB)$), the two ROIs were considered to be the same cell (Rose et al., 2016) (Figure S4D-G). The index numbers in each experiment were paired for such cells. Failure to track cells across imaging days could be due to (1) shifts on the x, y axis in the imaging field; (2) cells not segmented in one day but segmented in the other day; (3) cells out of focus in one day and (4) same cells but ROI intersection <50% of ROI union (Figure S4J). Reason (2) accounts for most of the differences between ROI maps, and this is because only 2-4% of the full imaging movie was used to build the pixel-wise correlation maps used for cell segmentation (again, limited by GPU performance). Because the visual stimulus movies are presented in pseudo-random sequence, different sequences will be viewed at one day or the next. Thus, some visually responsive cells may not have responded during the roughly 800 frames used to compute the correlation maps. After the cells tracked in P22-P29 and P29-P36 were identified, cells tracked across P22-P29-P36 were identified by intersecting P22-P29 and P29-P36 index pairs (Figure S4H, I), and index numbers in each day for these cells were concatenated as a matrix. Overall, 56 ± 6% of cells segmented on P36 were also segmented on P22 and P29 in normally reared mice, 47 ± 9% of cells segmented on P36 were also segmented on P22 and P29 in dark-reared mice. This is a significantly better than the 35 ± 3% in Wagner et al., 2019.

Analysis of longitudinal data: Using the index matrix, each neuron's functional class (unresponsive, monocular and binocular) and receptive field tuning properties measured for each eye and across days was assembled as a separate matrix.

Experiments on effects of imaging focal plane displacement on the overlap of masks of segmented cells and on receptive field tuning: The effect of focal plane offsets on our measures of receptive field tuning and binocularity is examined in Figure S5. In these control experiments, consistency in segmenting cells and in their receptive field tuning was measured as the focal plane was shifted up or down in 5μm steps over a range of 15μm. This was done across five mice. Consistency in segmenting cells refers to the overlap in segmented cells between two focal planes. For example, segmenting cells at one focal plane and then at a second focal plane above or below the original will give two segmentation

masks. The overlap of these two masks will become progressively smaller as the difference in focal plane offset increases. This overlap is measured as the Jaccard index, which is the size of the intersection of these two masks divided by the size of their union. As an example, consider an experiment in which 100 cells are segmented from one focal plane and 110 cells are segmented from another, and 80 of these cells are found to overlap between the two experiments; the Jaccard index is 80/(80+(100-80)+(110-80)) = 0.615.

The Jaccard index and measures of receptive field tuning stability as a function of focal plane offset were made from a total of 9 experiments using 5 mice (details are shown in the table below). In each experiment, measures of visually evoked responses were consecutively taken at 4 focal planes. For four experiments (2, 5, 7, 9 in the table below), response measurements were first taken at focal plane N. These measures were then repeated again at focal plane N (named N' hereafter) and then at focal planes N−5μm and N+10μm. Thus, six comparisons across focal planes can be considered: one comparison of delta = 0μm (N to N'), two comparisons of delta = 5μm (N to N−5μm and N' to N−5μm), two comparisons of delta = 10μm (N to N+10μm and N' to N+10μm), and one comparison of delta = 15μm (N −5μm to N+10μm). To minimize experimental design bias and to collect sufficient data for delta = 0μm and delta = 15μm, we performed additional experiments at N, N', N+5μm, N −10μm (experiments 3 and 8), N, N', N−5μm, N−10μm (experiment 1), and N, N', N", N+/ −15μm (experiments 4 and 6, respectively).

Comparisons of different delta in these experiments are made with the same logic. These comparisons from 5 mice are listed here:

Experiment	mouse	Imaging age	Depth in 1st/ μm	Depth in 2nd/ μm	Depth in 3rd/ μm	Depth in 4th/ μm	Data points of pairwise cell intersection/union
1	1	P41	−224	−224	−229	−234	1 d=0, 3 d=5, 2 d=10
2	2	P53	−204	−204	−209	−194	1 d=0, 2 d=5, 2 d=10, 1 d=15
3	3, plane1	P21	−167	−167	−162	−177	1 d=0, 2 d=5, 2 d=10, 1 d=15
4	3, plane2	P22	−186	−186	−186	−171	3 d=0, 3 d=15
5	4, plane1	P22	−179	−179	−184	−169	1 d=0, 2 d=5, 2 d=10, 1 d=15
6	4, plane2	P23	−149	−149	−149	−164	3 d=0, 3 d=15
7	5, plane1	P31	−193	−193	−198	−183	1 d=0, 2 d=5, 2 d=10, 1 d=15
8	5, plane2	P32	−222	−222	−217	−232	1 d=0, 2 d=5, 2 d=10, 1 d=15
9	5, plane3	P33	−163	−163	−168	−153	1 d=0, 2 d=5, 2 d=10, 1 d=15
						Total :	13 d=0, 15 d=5, 14 d=10, 12 d=15

Figure plotting

Density profile plots: The code for calculating density profiles was modified from Matlab code scattercloud (https://www.mathworks.com/matlabcentral/fileexchange/6037-scattercloud). Briefly, we first made same number of bins (n=11~16) along both the x- and y-axis, for pairs of measurements we used as scatter plot. We then calculated density of data

points in each bin to get an n-by-n density profile matrix and plot the matrix using Matlab surf function with interpolated coloring for each face. Then we made scatter plot on top of the density profile plot.

Density profiles overlay: We overlaid pairs of density profiles by using Matlab imfuse function. Before overlaying two matrices, we normalized each matrix to make the maximum density to be 1 and minimum density to be 0, so that two density profiles being merged are in the same scale.

Violin plots: We used violin plot function (https://github.com/bastibe/Violinplot-Matlab) to make all our violin plots.

Alluvial flow diagram: We used alluvialflow function to generate the diagram in Figure S5C (https://www.mathworks.com/matlabcentral/fileexchange/66746-alluvial-flow-diagram).

QUANTIFICATION AND STATISTICAL ANALYSIS

A power analysis was not performed a-priori to determine sample size. All statistical analyses were performed in Matlab (www.mathworks.com), using non-parametric tests with significance levels set at $\alpha < 0.05$, and did Bonferroni corrections on α for multiple comparisons when necessary. Mann-Whitney U-tests (Wilcoxon rank sum test) were used to test differences between two independent populations. When comparing more than two populations that were non-normally distributed, a Kruskal-Wallis test, a nonparametric version of one-way ANOVA, was used to determine whether statistically significant differences existed among these independent populations. If significant differences did exist, post hoc multiple comparison tests (multcompare in Matlab) with Bonferroni correction were used to test for significant differences between pairs within the group. To compare more than two proportions (Figure 1F), Tukey's HSD multiple comparisons test among proportions were used (https://www.mathworks.com/matlabcentral/fileexchange/15499-tmcomptest). For pairwise comparisons of proportions (Figure 6B), Chi-square test was used https://www.mathworks.com/matlabcentral/fileexchange/45966-compare-two-proportions-chi-square).

Supplementary Material

Refer to Web version on PubMed Central for supplementary material.

Acknowledgments:

We thank all members in the Zipursky lab and Trachtenberg lab. S.L.Z. thanks Tom Mrsic-Flogel and Sonja Hofer for hosting him during a sabbatical during which part of this paper was written.

Funding: NIH R01 EY023871 and NIH R01 EY027407 (J.T.T.), NIH R01 NS116471 and NIH EB022915 (D.L.R.). We thank W. M. Keck Foundation for funding this project. S.L.Z. is an investigator of Howard Hughes Medical Institute.

References

Ackman JB, Burbridge TJ, and Crair MC (2012). Retinal waves coordinate patterned activity throughout the developing visual system. Nature 490, 219–225. [PubMed: 23060192]

Adesnik H, Bruns W, Taniguchi H, Huang ZJ, and Scanziani M (2012). A neural circuit for spatial summation in visual cortex. Nature 490, 226–230. [PubMed: 23060193]

Berens P, Freeman J, Deneux T, Chenkov N, McColgan T, Speiser A, Macke JH, Turaga SC, Mineault P, Rupprecht P, et al. (2018). Community-based benchmarking improves spike rate inference from two-photon calcium imaging data. PLOS Comput. Biol 14, e1006157. [PubMed: 29782491]

Bi GQ, and Poo MM (1998). Synaptic modifications in cultured hippocampal neurons: Dependence on spike timing, synaptic strength, and postsynaptic cell type. J. Neurosci 18, 10464–10472. [PubMed: 9852584]

Chen T-W, Wardill TJ, Sun Y, Pulver SR, Renninger SL, Baohan A, Schreiter ER, Kerr RA, Orger MB, Jayaraman V, et al. (2013). Ultrasensitive fluorescent proteins for imaging neuronal activity. Nature 499, 295–300. [PubMed: 23868258]

Crair MC, Gillespie DC, and Stryker MP (1998). The role of visual experience in the development of columns in cat visual cortex. Science (80-.). 279, 566–570.

Daigle TL, Madisen L, Hage TA, Valley MT, Knoblich U, Larsen RS, Takeno MM, Huang L, Gu H, Larsen R, et al. (2018). A Suite of Transgenic Driver and Reporter Mouse Lines with Enhanced Brain-Cell-Type Targeting and Functionality. Cell 174, 465–480.e22. [PubMed: 30007418]

Debanne D, Gahwiler BH, and Thompson SM (1998). Long-term synaptic plasticity between pairs of individual CA3 pyramidal cells in rat hippocampal slice cultures. J. Physiol 507, 237–247. [PubMed: 9490845]

Espinosa JS, and Stryker MP (2012). Development and Plasticity of the Primary Visual Cortex. Neuron 75, 230–249. [PubMed: 22841309]

Faguet J, Maranhao B, Smith SL, and Trachtenberg JT (2009). Ipsilateral Eye Cortical Maps Are Uniquely Sensitive to Binocular Plasticity. J. Neurophysiol 101, 855–861. [PubMed: 19052109]

Fawcett SL, Wang YZ, and Birch EE (2005). The critical period for susceptibility of human stereopsis. Investig. Ophthalmol. Vis. Sci 46, 521–525. [PubMed: 15671277]

Feldman DE (2012). The Spike-Timing Dependence of Plasticity. Neuron 75, 556–571. [PubMed: 22920249]

Freeman RD, and Olson C (1982). Brief periods of monocular deprivation in kittens: Effects of delay prior to physiological study. J. Neurophysiol 47, 139–150. [PubMed: 7062093]

Garrett ME, Nauhaus I, Marshel JH, and Callaway EM (2014). Topography and Areal Organization of Mouse Visual Cortex. J. Neurosci 34, 12587–12600. [PubMed: 25209296]

Gordon JA, and Stryker MP (1996). Experience-dependent plasticity of binocular responses in the primary visual cortex of the mouse. J. Neurosci 16, 3274–3286. [PubMed: 8627365]

Gouwens NW, Sorensen SA, Berg J, Lee C, Jarsky T, Ting J, Sunkin SM, Feng D, Anastassiou CA, Barkan E, et al. (2019). Classification of electrophysiological and morphological neuron types in the mouse visual cortex. Nat. Neurosci 22, 1182–1195. [PubMed: 31209381]

Gu Y, and Cang J (2016). Binocular matching of thalamocortical and intracortical circuits in the mouse visual cortex. Elife 5, 1–14.

Hooks BM, and Chen C (2020). Circuitry Underlying Experience-Dependent Plasticity in the Mouse Visual System. Neuron 106, 21–36. [PubMed: 32272065]

Hoy JL, and Niell CM (2015). Layer-specific refinement of visual cortex function after eye opening in the awake mouse. J. Neurosci 35, 3370–3383. [PubMed: 25716837]

Hubel DH, and Wiesel TN (1962). Receptive fields, binocular interaction and functional architecture in the cat's visual cortex. J. Physiol 160, 106–154. [PubMed: 14449617]

Hubel DH, and Wiesel TN (1968). Receptive fields and functional architecture of monkey striate cortex. J. Physiol 195, 215–243. [PubMed: 4966457]

HUBEL DH, and WIESEL TN (1963). RECEPTIVE FIELDS OF CELLS IN STRIATE CORTEX OF VERY YOUNG, VISUALLY INEXPERIENCED KITTENS. J. Neurophysiol 26, 994–1002. [PubMed: 14084171]

Jimenez LO, Tring E, Trachtenberg JT, and Ringach DL (2018). Local tuning biases in mouse primary visual cortex. J. Neurophysiol 120, 274–280. [PubMed: 29668380]

Kalatsky VA, and Stryker MP (2003). New Paradigm for Optical Imaging: Temporally Encoded Maps of Intrinsic Signal. Neuron 38, 529–545. [PubMed: 12765606]

Katz LC, and Shatz CJ (1996). Synaptic Activity and the Construction of Cortical Circuits. Science (80-.). 274, 1133–1138.

Kim EJ, Juavinett AL, Kyubwa EM, Jacobs MW, and Callaway EM (2015). Three Types of Cortical Layer 5 Neurons That Differ in Brain-wide Connectivity and Function. Neuron 88, 1253–1267. [PubMed: 26671462]

Ko H, Cossell L, Baragli C, Antolik J, Clopath C, Hofer SB, and Mrsic-Flogel TD (2013). The emergence of functional microcircuits in visual cortex. Nature 496, 96–100. [PubMed: 23552948]

Ko H, Mrsic-Flogel TD, and Hofer SB (2014). Emergence of Feature-Specific Connectivity in Cortical Microcircuits in the Absence of Visual Experience. J. Neurosci 34, 9812–9816. [PubMed: 25031418]

Lazarus MS, Huang ZJ, Ali A, Thomson A, Ango F, Wu C, Van der Want, J., Wu P, Schachner M, Huang Z, et al. (2011). Distinct maturation profiles of perisomatic and dendritic targeting GABAergic interneurons in the mouse primary visual cortex during the critical period of ocular dominance plasticity. J. Neurophysiol 106, 775–787. [PubMed: 21613595]

Li Y, Van Hooser SD, Mazurek M, White LE, and Fitzpatrick D (2008). Experience with moving visual stimuli drives the early development of cortical direction selectivity. Nature 456, 952–956. [PubMed: 18946471]

Liu CH, Heynen AJ, Shuler MGH, and Bear MF (2008). Cannabinoid Receptor Blockade Reveals Parallel Plasticity Mechanisms in Different Layers of Mouse Visual Cortex. Neuron 58, 340–345. [PubMed: 18466745]

Madisen L, Zwingman TA, Sunkin SM, Oh SW, Zariwala HA, Gu H, Ng LL, Palmiter RD, Hawrylycz MJ, Jones AR, et al. (2010). A robust and high-throughput Cre reporting and characterization system for the whole mouse brain. Nat. Neurosci 13, 133–140. [PubMed: 20023653]

Markram H, Lubke J, Frotscher M, and Sakmann B (1997). Regulation of synaptic efficacy by coincidence of postsynaptic APs and EPSPs. Science (80-.). 275, 213–215.

Mayford M, Bach ME, Huang YY, Wang L, Hawkins RD, and Kandel ER (1996). Control of memory formation through regulated expression of a CaMKII transgene. Science 274, 1678–1683. [PubMed: 8939850]

Mineault PJ, Tring E, Trachtenberg JT, and Ringach DL (2016). Enhanced Spatial Resolution During Locomotion and Heightened Attention in Mouse Primary Visual Cortex. J. Neurosci 36, 6382–6392. [PubMed: 27307228]

Niell CM (2015). Cell Types, Circuits, and Receptive Fields in the Mouse Visual Cortex. Annu. Rev. Neurosci 38, 413–431. [PubMed: 25938727]

Ohzawa I, Deangelis GC, and Freeman RD (1997a). Encoding of Binocular Disparity by Complex Cells in the Cat's Visual Cortex. J. Neurophysiol 77, 2879–2909. [PubMed: 9212245]

Ohzawa I, DeAngelis GC, and Freeman RD (1997b). The neural coding of stereoscopic depth. Neuroreport 8, iii–xii.

Pachitariu M, Stringer C, and Harris KD (2018). Robustness of spike deconvolution for neuronal calcium imaging. J. Neurosci 38, 7976–7985. [PubMed: 30082416]

Paik S-B, and Ringach DL (2011). Retinal origin of orientation maps in visual cortex. Nat. Neurosci 14, 919–925. [PubMed: 21623365]

Priebe NJ (2016). Mechanisms of Orientation Selectivity in the Primary Visual Cortex. Annu. Rev. Vis. Sci 2, 85–107. [PubMed: 28532362]

Priebe NJ, and McGee AW (2014). Mouse vision as a gateway for understanding how experience shapes neural circuits. Front. Neural Circuits 8, 123. [PubMed: 25324730]

Ringach DL (2004). Haphazard Wiring of Simple Receptive Fields and Orientation Columns in Visual Cortex. J. Neurophysiol 92, 468–476. [PubMed: 14999045]

Ringach DL, Hawken MJ, and Shapley R (1997). Dynamics of orientation tuning in macaque primary visual cortex. Nature 387, 281–284. [PubMed: 9153392]

Ringach DL, Shapley RM, and Hawken MJ (2002). Orientation selectivity in macaque V1: Diversity and laminar dependence. J. Neurosci 22, 5639–5651. [PubMed: 12097515]

Ringach DL, Mineault PJ, Tring E, Olivas ND, Garcia-Junco-Clemente P, and Trachtenberg JT (2016). Spatial clustering of tuning in mouse primary visual cortex. Nat. Commun 7.

Rose T, Jaepel J, Hübener M, and Bonhoeffer T (2016). Cell-specific restoration of stimulus preference after monocular deprivation in the visual cortex. Science 352, 1319–1322. [PubMed: 27284193]

Salinas KJ, Figueroa Velez DX, Zeitoun JH, Kim H, and Gandhi SP (2017). Contralateral Bias of High Spatial Frequency Tuning and Cardinal Direction Selectivity in Mouse Visual Cortex. J. Neurosci 37, 10125–10138. [PubMed: 28924011]

Sanes JR, and Zipursky SL (2020). Synaptic Specificity, Recognition Molecules, and Assembly of Neural Circuits. Cell 181, 536–556. [PubMed: 32359437]

Sarnaik R, Wang BS, and Cang J (2014). Experience-dependent and independent binocular correspondence of receptive field subregions in mouse visual cortex. Cereb. Cortex 24, 1658–1670. [PubMed: 23389996]

Shatz CJ, and Stryker MP (1978). Ocular dominance in layer IV of the cat's visual cortex and the effects of monocular deprivation. J. Physiol 281, 267–283. [PubMed: 702379]

Sherk H, and Stryker MP (1976). Quantitative study of cortical orientation selectivity in visually inexperienced kitten. J. Neurophysiol 39, 63–70. [PubMed: 1249604]

Skottun BC, De Valois RL, Grosof DH, Movshon JA, Albrecht DG, and Bonds AB (1991). Classifying simple and complex cells on the basis of response modulation. Vision Res. 31, 1078–1086.

Smith SL, and Trachtenberg JT (2007). Experience-dependent binocular competition in the visual cortex begins at eye opening. Nat. Neurosci 10, 370–375. [PubMed: 17293862]

Smith GB, Sederberg A, Elyada YM, Van Hooser SD, Kaschube M, and Fitzpatrick D (2015). The development of cortical circuits for motion discrimination. Nat. Neurosci 18, 252–261. [PubMed: 25599224]

Song S, Miller KD, and Abbott LF (2000). Competitive Hebbian learning through spike-timing-dependent synaptic plasticity. Nat. Neurosci 3, 919–926. [PubMed: 10966623]

Tasic B, Yao Z, Graybuck LT, Smith KA, Nguyen TN, Bertagnolli D, Goldy J, Garren E, Economo MN, Viswanathan S, et al. (2018). Shared and distinct transcriptomic cell types across neocortical areas. Nature 563, 72–78. [PubMed: 30382198]

Trachtenberg JT, Trepel C, and Stryker MP (2000). Rapid extragranular plasticity in the absence of thalamocortical plasticity in the developing primary visual cortex. Science (80-.). 287, 2029–2032.

Urban-Ciecko J, and Barth AL (2016). Somatostatin-expressing neurons in cortical networks. Nat. Rev. Neurosci 17, 401–409. [PubMed: 27225074]

van Versendaal D, and Levelt CN (2016). Inhibitory interneurons in visual cortical plasticity. Cell. Mol. Life Sci 73, 3677–3691. [PubMed: 27193323]

Wagner MJ, Kim TH, Kadmon J, Nguyen ND, Ganguli S, Schnitzer MJ, and Luo L (2019). Shared Cortex-Cerebellum Dynamics in the Execution and Learning of a Motor Task. Cell 177, 669–682.e24. [PubMed: 30929904]

Wang BS, Sarnaik R, and Cang J (2010). Critical Period Plasticity Matches Binocular Orientation Preference in the Visual Cortex. Neuron 65, 246–256. [PubMed: 20152130]

Wang BS, Feng L, Liu M, Liu X, and Cang J (2013). Environmental Enrichment Rescues Binocular Matching of Orientation Preference in Mice that Have a Precocious Critical Period. Neuron 80, 198–209. [PubMed: 24012279]

Wekselblatt JB, Flister ED, Piscopo DM, and Niell CM (2016). Large-scale imaging of cortical dynamics during sensory perception and behavior. J. Neurophysiol 115, 2852–2866. [PubMed: 26912600]

White LE, and Fitzpatrick D (2007). Vision and cortical map development. Neuron 56, 327–338. [PubMed: 17964249]

White LE, Coppola DM, and Fitzpatrick D (2001). The contribution of sensory experience to the maturation of orientation selectivity in ferret visual cortex. Nature 411, 1049–1052. [PubMed: 11429605]

WIESEL TN, and HUBEL DH (1963). SINGLE-CELL RESPONSES IN STRIATE CORTEX OF KITTENS DEPRIVED OF VISION IN ONE EYE. J. Neurophysiol 26, 1003–1017. [PubMed: 14084161]

Wilson NR, Runyan CA, Wang FL, and Sur M (2012). Division and subtraction by distinct cortical inhibitory networks in vivo. Nature 488, 343–348. [PubMed: 22878717]

Xu H. ping, Furman M, Mineur YS, Chen H, King SL, Zenisek D, Zhou ZJ, Butts DA, Tian N, Picciotto MR, et al. (2011). An Instructive Role for Patterned Spontaneous Retinal Activity in Mouse Visual Map Development. Neuron 70, 1115–1127. [PubMed: 21689598]

Xu X, Cang J, and Riecke H (2020). Development and binocular matching of orientation selectivity in visual cortex: a computational model. J. Neurophysiol 123, 1305–1319. [PubMed: 31913758]

Yaeger CE, Ringach DL, and Trachtenberg JT (2019). Neuromodulatory control of localized dendritic spiking in critical period cortex. Nature 567, 100–104. [PubMed: 30787434]

Yavorska I, and Wehr M (2016). Somatostatin-Expressing Inhibitory Interneurons in Cortical Circuits. Front. Neural Circuits 10, 76. [PubMed: 27746722]

Highlights

- Improvements in ipsilateral eye tuning change binocularity during the critical period
- Poorly tuned binocular neurons are rendered monocular
- Conversion of sharply tuned monocular neurons establishes new binocular neurons
- Vision drives this sharpening and binocular conversion in layer 2/3 and not 4

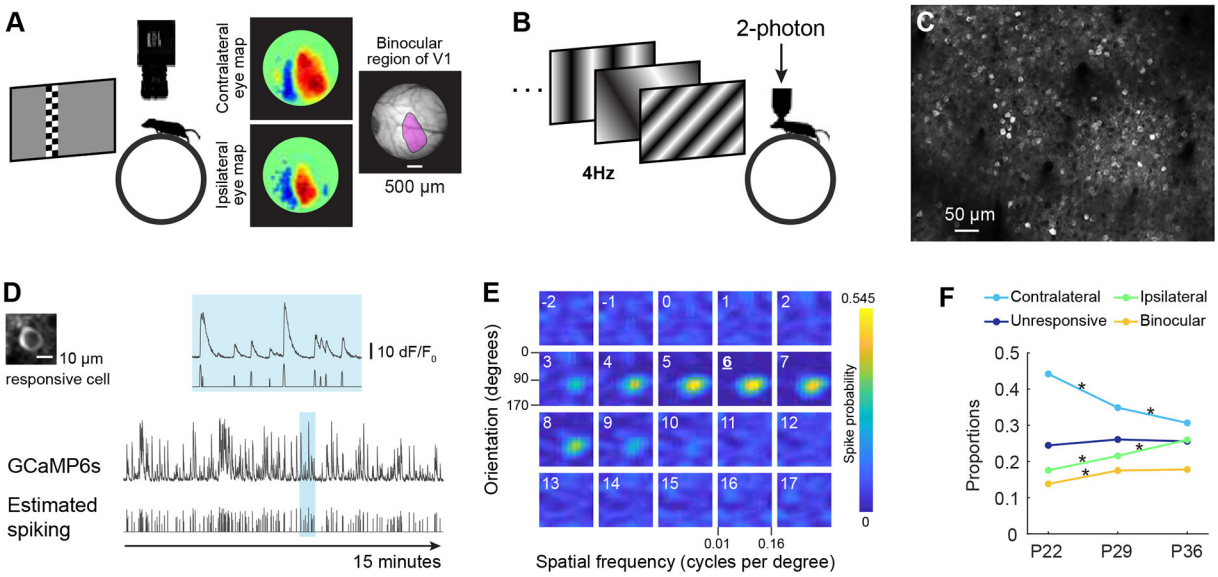

Figure 1. Binocular field mapping and receptive field tuning.

(**A**) Visual field maps obtained from low-magnification epifluorescence imaging of GCaMP6s evoked responses to checkerboard bars, which were both drifting and flashing, presented to each eye separately. Red and blue colors in eye-specific maps represent opposite visual field signs designating separate visual areas, with the red sign designating V1 here. The purple shading in the vascular image on the right identifies the binocular region of V1.

(**B**) Schematic of 2-photon imaging of visually evoked GCaMP6s responses to a series of sinusoidal gratings sequentially presented at 4Hz.

(**C**) Example of a field of view of GCaMP6s labeled neurons in binocular visual cortex.

(**D**) Example of fluorescence changes and estimated spike rate over 15 minutes. The cell is shown in the upper left. The narrow blue highlighted region in the full traces has been expanded horizontally and displayed above for clarity. Scale bar for fluorescence changes is shown to the right of this expanded trace. Example is from responses to contralateral eye stimulation.

(**E**) Spike probability as a function of stimulus onset for the cell in panel D. Maps are derived from 18 orientations at 12 spatial frequencies presented 16 to 17 times. Numbers in the top left indicate frames relative to stimulus onset. For this cell, peak response occurs 6 imaging frames, or 387 ms after onset of its optimal stimuli.

(**F**) Proportions of monocular, binocular and unresponsive neurons as a function of age, for all L2/3 neurons imaged in NR mice across the critical period. * indicate significant changes. Statistics: Tukey's HSD multiple comparisons test among proportions.

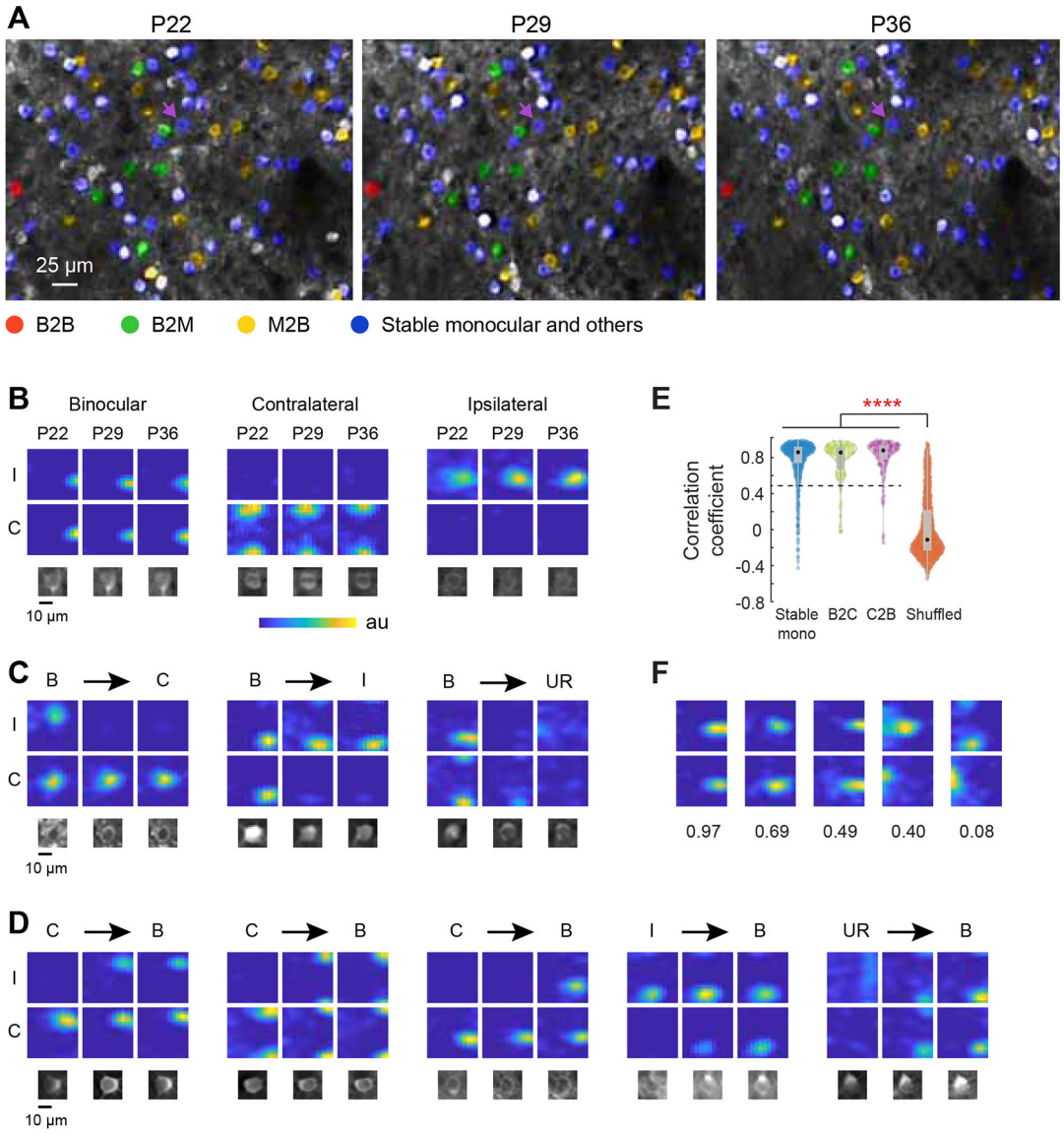

Figure 2. Longitudinal tracking of receptive field tuning properties.

(**A**) Partial field of view of longitudinal imaging in layer 2/3 across the critical period. Cells tracked for tuning properties across all three time points are colored, with red, green and yellow masks represent stable binocular neurons (B2B), lost binocular neurons (B2M) and binocular neurons recruited from monocular/unresponsive pools (M2B). Blue masks indicate stable monocular neurons or neurons with other trajectories. Cells without color masks (white) are ones with tuning properties not tracked. Purple arrows highlight the stable ipsilateral neuron shown in B.

(**B**) Example of tuning kernels of neurons that were stable over all three time points. I: ipsilateral eye stimulation; C: contralateral eye stimulation. Below each kernel is an image of the cell at each time point. Ordinate, orientation from 0° to 170°. Abscissa, spatial frequency from 0.01 to 0.16 cycles/degree. Color indicates estimated spiking at each possible combination of orientation and spatial frequency. Color map of estimated spiking is

normalized for each cell. The contralateral neuron has orientation preference close to 0°, thus its kernels are split at the top and bottom.

(**C**) Kernels are plotted as in B, but for binocular neurons that become monocular or unresponsive. B, binocular; C, monocular contralateral; I, monocular ipsilateral; UR, unresponsive.

(**D**) Kernels are plotted as in B, but for monocular or unresponsive neurons that become binocular.

(**E**) Correlation coefficient comparing tuning kernel stability between stable monocular cells (stable mono), binocular neurons that become contralateral (B2C) and contralateral neurons becoming binocular (C2B), and cells that paired by chance across the critical period. The tapered tail extending towards higher coefficients in the shuffled control reflects random pairing of kernels with high circular variance (>0.7) and low spatial frequency preference (<0.02 cycles/degree). Statistical test: Kruskal-Wallis one-way analysis of variance, with **** indicating p-value below 1.0e-5. Black brackets denote significance using multiple comparison test with Bonferroni correction for pairwise comparisons. Stable mono: n = 854; B2C: n = 84; C2B: n = 138; Shuffled: n = 1541. This is similar for dark-reared animals (not shown).

(**F**) Matching coefficients for five pairs of tuning kernels, presented in order of decreasing coefficients. The value of matching coefficient is below each pair.

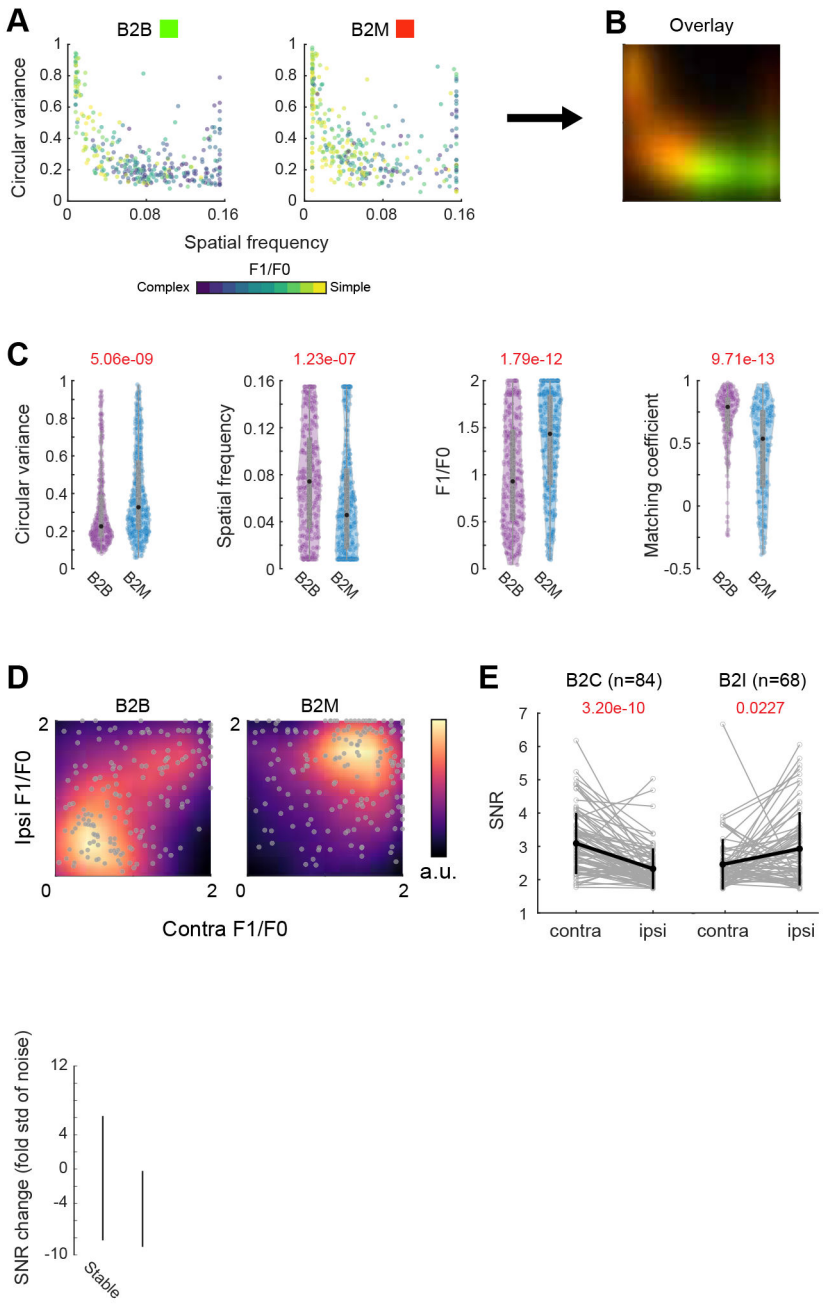

Figure 3. Poorly tuned binocular neurons lose responsiveness to one eye and become monocular.

(**A**) Tuning measures for binocular neurons retained or lost between P22-29 or P29-36. Each dot represents response with circular variance, spatial frequency and F1/F0 (color bar) to contralateral or ipsilateral eye of a binocular neuron prior to the retention (B2B; 170 neurons) or loss (B2M; 182 neurons) of binocularity.

(**B**) Overlay of the tuning density profiles of binocular neurons from (A). Cells that remained binocular (green) have higher spatial frequency and lower circular variance than those rendered monocular (red).

(**C**) Receptive field tuning measurements and matching coefficients of stable (B2B; 170 neurons) and lost binocular neurons (B2M; 182 neurons), prior to the transition. Black dot, median; gray vertical line, quartiles with whiskers extending to 2.698σ. P-values, Mann-Whitney U-test.

(**D**) F1/F0 plots for the ipsilateral and contralateral eye evoked responses of stable (B2B) and lost binocular neurons (B2M) prior to the transition. Color bar, density. Cells in the lower left and upper right quadrants are “complex” and “simple”, respectively.

(**E**) SNR of responses to contralateral and ipsilateral eyes (contra and ipsi, respectively) of binocular neurons rendered monocular contralateral (B2C) or ipsilateral (B2I) prior to transition. Gray, measurements for individual neurons; black, mean ± standard deviation. P-values, Mann-Whitney U-test between contra and ipsi SNR for each group.

(**F**) Neurons experience large and discrete jumps in SNR as they lose responsiveness to an eye. Boxplots of SNR changes of tuning kernels. Plots compare the change in SNR before and after loss of responsiveness to the ipsilateral eye. Stable: changes in SNR for stably responsive, contralateral eye tuning kernels. Lost: SNR changes for the lost ipsilateral eye tuning kernels. Change is plotted as fold of std of noise SNR. Lost, n = 83; Stable, n = 516. P-values, Mann-Whitney U-test. P-values are corrected for multiple comparisons as the Stable pool is used again in Figure 4.

(**G**) Schematic showing that the fates of binocular neurons are determined by their tuning properties. B2B, binocular neurons that remain binocular; B2M, binocular neurons that become monocular. The width of the gaussian above the arrows reflects orientation tuning selectivity – narrower is more selective. Spatical frequency is depicted by the circle above the arrows – more lines indicates higher spatial frequency preferences. Responses from both eyes are maintained when tuning is sharper and spatial frequency preferences are higher (top), otherwise, responses to one eye are lost (bottom)

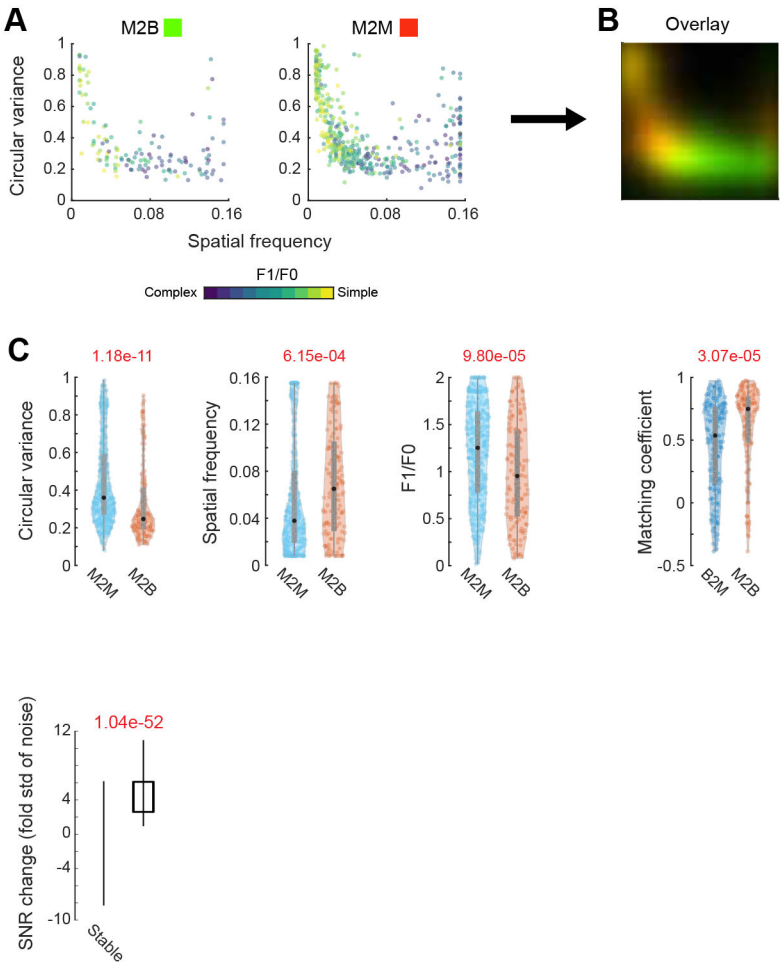

Figure 4. Sharply tuned monocular neurons gain matched responses from the other eye and become binocular.

(**A**) Tuning measures for monocular contralateral neurons which became binocular (M2B, 138 neurons) or remained monocular (M2M, 516 neurons) between P22-29 and P29-36. Each dot represents a cell with circular variance, spatial frequency and F1/F0 (color bar), prior to the transition.

(**B**) Tuning density profiles of monocular contralateral neurons. Cells that became binocular (M2B, green) have higher spatial frequency and lower circular variance than those that remained monocular (M2M, red).

(**C**) Receptive field tuning measurements in panel A, and matching coefficients for newly formed (M2B, n=138) and lost (B2M, n= 182) binocular neurons. Black dot, median; gray vertical lines, quartiles with whiskers extending to 2.698σ. P-values, Mann-Whitney U-test.

(**D**) Neurons experience large and discrete jumps in SNR as they gain responsiveness to an eye. Boxplots of SNR changes of tuning kernels. Stable: changes in SNR for stably responsive, contralateral eye tuning kernels. Gained: SNR changes for the newly-responsive ipsilateral eye tuning kernels. Change is plotted as fold of std of noise SNR. Gained, n = 136; Stable, n = 516. P-values, Mann-Whitney U-test. P-values are corrected for multiple comparisons as the Stable pool was used in Figure 3 as well.

(**E**) Schematic showing that the fates of monocular neurons are determined by their tuning properties. M2M, monocular neurons that remain monocular; M2B, monocular neurons that become binocular. The width of the gaussian above the arrows reflects orientation tuning selectivity – narrower is more selective. Spatial frequency is depicted by the circle above the arrows – more lines indicates higher spatial frequency preferences. Monocular neurons with broad orientation tuning and lower spatial frequency preferences remain monocular (top). Those with greater orientation tuning selectivity and higher spatial frequency preferences gain matched input from the other eye and become binocular (bottom)

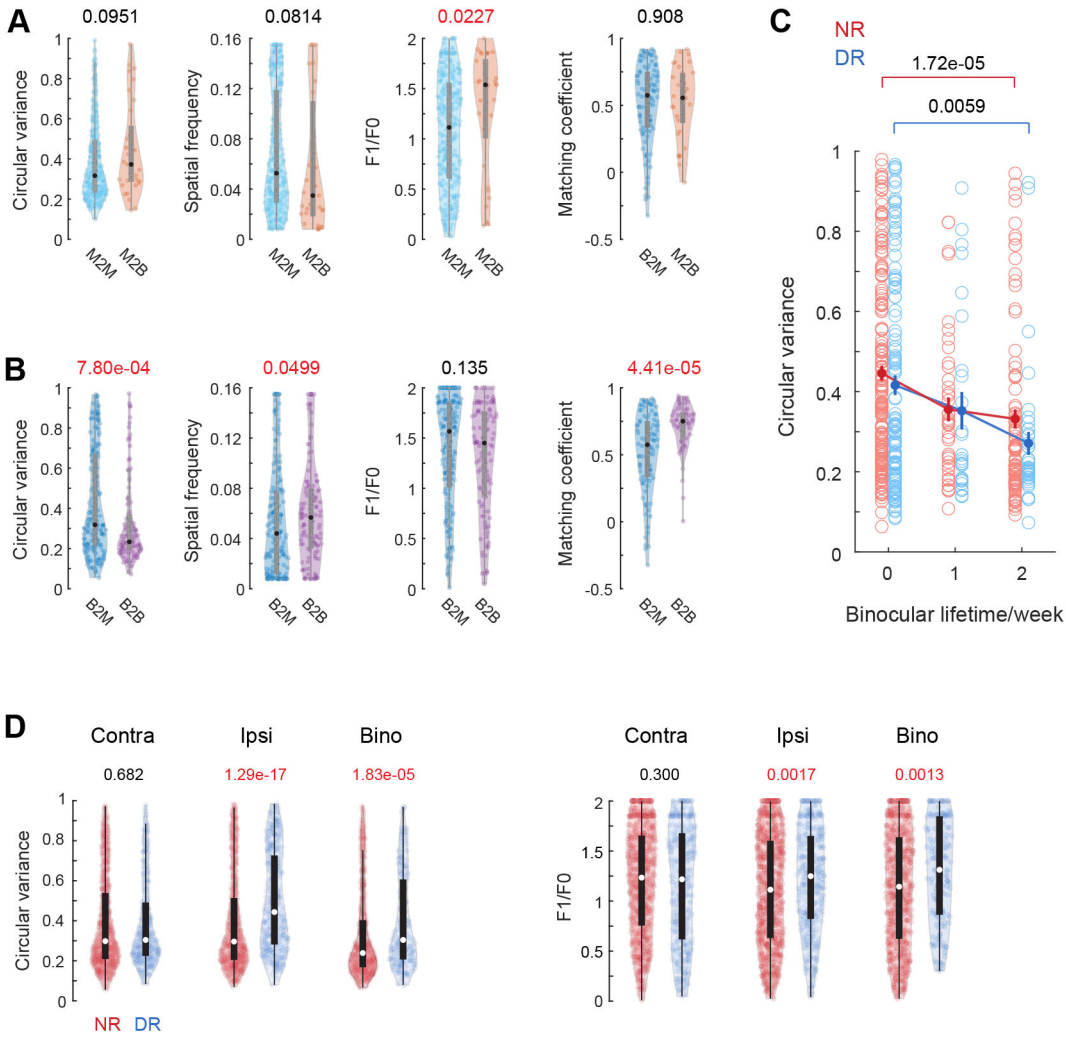

Figure 5. Vision is necessary for conversion of sharply tuned monocular neurons into binocular neurons.

(**A**) Receptive field tuning and matching coefficient measurements as in Figure 4C for dark reared (DR) mice. M2B, n = 33; B2M, n = 96; and M2M, n = 305.

(**B**) Receptive field tuning and matching coefficient measurements as in Figure 3C for DR mice. B2B, n =59; B2M, n = 96.

(**C**) Plot of circular variance as a function of binocular lifetime of neurons in normally reared (NR) and DR mice. Each circle represents response to contralateral or ipsilateral eye stimulation of a binocular neuron. Abscissa: 0, neuron was binocular at P22 but not at P29; 1, neuron was binocular at P22 and P29, but not P36; and 3, binocular at all three time points. For each condition (NR and DR), mean+/−SEM is plotted as dot and line at each lifetime. Mann-Whitney U-test with Bonferroni correction ($\alpha = 0.0167$) was used, with significant p-values shown above their pairwise comparisons. Sample number: NR: 160, 40, 88 from 0 to 2 weeks; DR: 118, 26, 38 from 0 to 2 weeks. No statistical difference exist between the distribution in circular variance for neurons from NR and DR for each binocular lifetime.

(**D**) Circular variance and F1/F0 for neurons imaged at P36 in NR and DR mice. “Contra” represents responses to contralateral eye from monocular contralateral and binocular neurons; “Ipsi” represents responses to ipsilateral eye from monocular ipsilateral and binocular neurons; “Bino” represents responses to contralateral or ipsilateral eye from binocular neurons. White dot, median; black vertical lines, quartiles with whiskers extending to 2.698σ. NR Contra, n = 923; DR Contra, n = 404; NR Ipsi, n = 834; DR Ipsi, n = 459; NR Bino, n = 678; DR Bino, n = 156. P-values, Mann-Whitney U-test comparison between NR and DR.

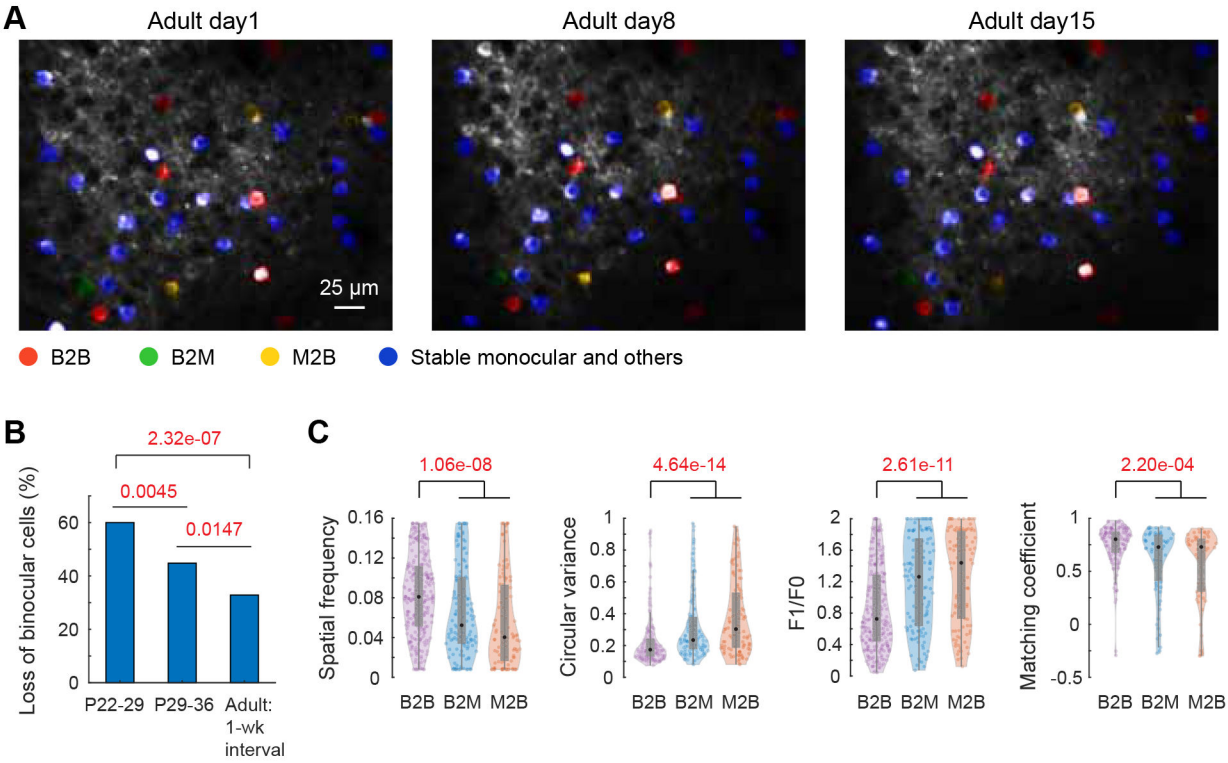

Figure 6. Binocular pools change but tuning properties do not in adult L2/3 neurons.

(**A**) Partial field of view of adult layer 2/3 neurons longitudinally imaged. Cells tracked for tuning properties across all three time points are colored, with red, green and yellow masks representing stable binocular neurons (B2B), lost binocular neurons (B2M) and binocular neurons recruited from monocular/unresponsive pools (M2B). Blue masks indicate stable monocular neurons or neurons with other trajectories. Cells without color masks are ones with tuning properties not tracked.

(**B**) Increased stability of binocular neurons in adult. The fraction of binocular neurons lost during a week is: B2M/(B2B+B2M)). Chi-square test for pairwise comparisons; P values, red; Bonferroni corrected, $\alpha = 0.0167$.

(**C**) Tuning measurements of contralateral or ipsilateral eye for stable, lost and new binocular neurons (B2B, B2M and M2B, respectively). For B2B and B2M, measurements prior to transition are plotted; for M2B, measurements post-transition are plotted. Black dots, median; gray vertical lines, quartiles with whiskers extending to 2.698σ. B2B: n =137; B2M: n = 67; M2B: n = 54. Statistics: Kruskal-Wallis one-way analysis of variance, with significant p-values shown above each group in red. Black brackets denote significance using multiple comparison test with Bonferroni correction for pairwise comparisons. Note no difference between B2M and M2B.

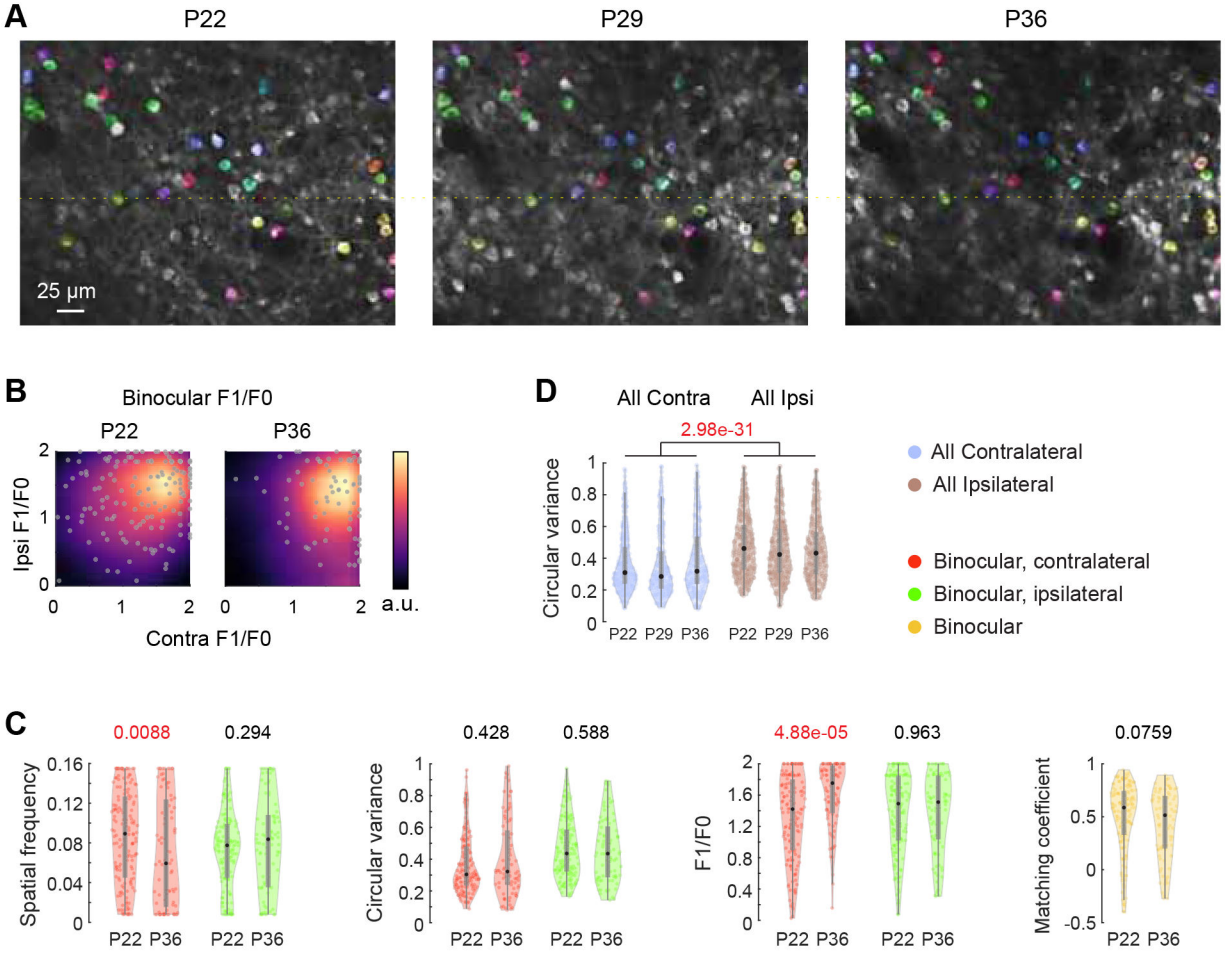

Figure 7. Binocular tuning in layer 4 does not improve across the critical period.

(**A**) Partial field of view in layer 4 imaged longitudinally at P22, P29, and P36. Longitudinally tracked cells are colored arbitrarily. A dotted line was added to facilitate visual inspection.

(**B**) F1/F0 plots of binocular neurons among longitudinally imaged layer 4 cells at P22 (n=155) and P36 (n=85). Color bar, density (arbitrary units). Upper right and lower left quadrants represent “simple” and “complex” cells, respectively.

(**C**) Tuning measurements of binocular neurons at P22 and P36. Color codes are shown to the right of panel D. Black dots, median; gray vertical lines, quartiles with whiskers extending to 2.698σ. P-values (red), Mann-Whitney U-test are shown above each pair of comparisons.

(**D**) Circular variance for all contralateral and ipsilateral responses at each age of longitudinally imaged L4 neurons. Statistics: Kruskal-Wallis one-way analysis of variance, with significant p-value shown in red. Black bracket denotes significance using multiple comparison test with Bonferroni correction for pairwise comparisons. P22: 367 contra, 350 ipsi; P29: 278 contra, 352 ipsi; P36, 215 contra, 290 ipsi.

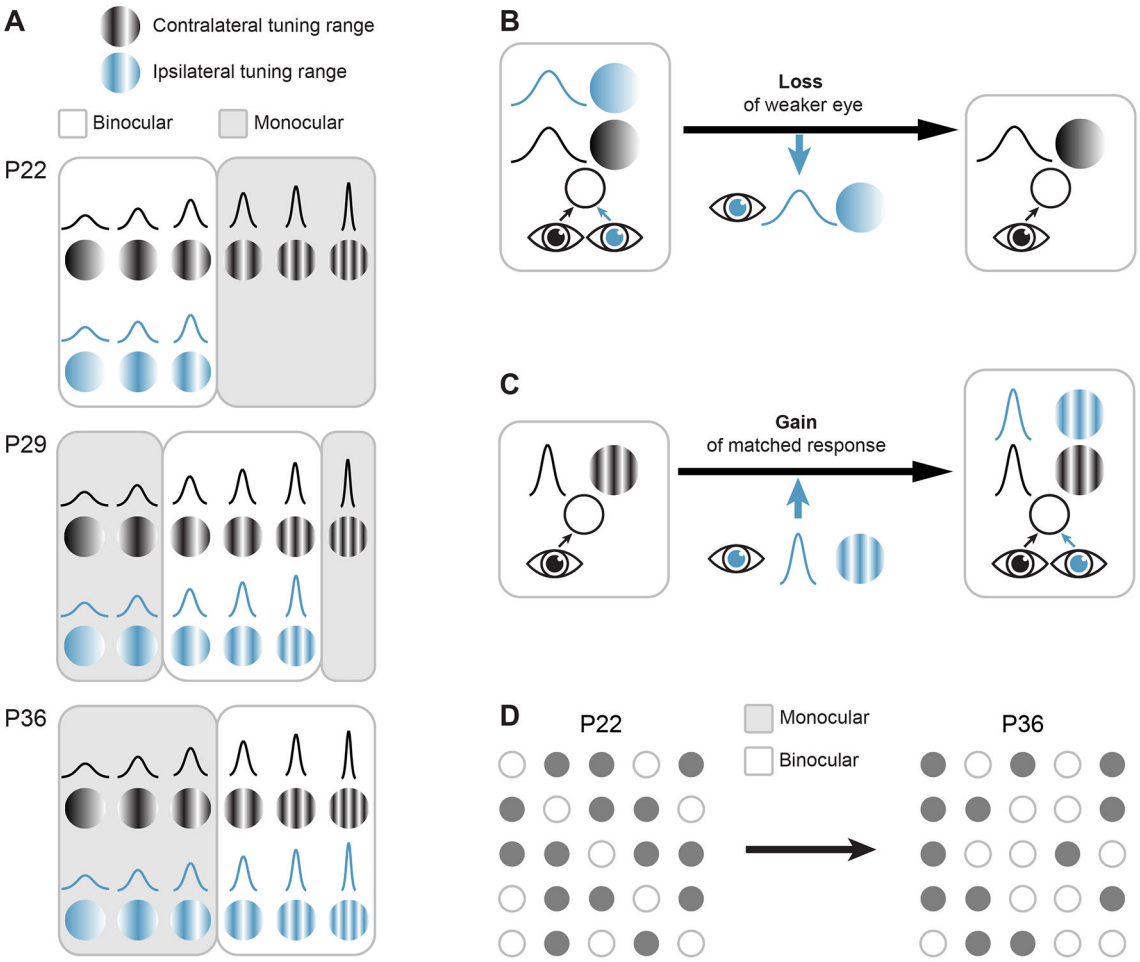

Figure 8. Schematic outline of the gain and elimination of binocular cells as ipsilateral eye tuning sharpens.

(A) At P22, reptive field tuning of contralateral eye responses (black/white) are mature and span the full range of orientation and spatial frequencies. Ipsilateral eye tuning (blue/white), however, is characterized by broad tuning and lower spatial frequencies. Binocular neurons reflect this tuning. By P29, ipsilateral eye tuning has matured. Binocular tuning now reflects this sharper ipsilateral eye tuning. Binocular neurons with poorer tuning are rendered monocular. By P36, ipsilateral eye tuning is fully mature and this, again, is reflected in binocular tuning. Again, poorer tuned binocular neurons are rendered monocular.

(B) Schematic of the conversion of poorly tuned binocular neurons to monocular. The weaker eye is lost.

(C) Schematic of the conversion of sharply tuned monocular neurons to binocular. Sharply tuned monocular neurons gain responses to the other eye and these new responses precisely match the tuning of the host.

(D) Schematic illustrating the change in the cellular composition of the binocular pool from P22 (critical period opening) to P36 (critical period closure).

KEY RESOURCES TABLE

REAGENT or RESOURCE	SOURCE	IDENTIFIER
Antibodies		
Rabbit monoclonal anti-Snail	Cell Signaling Technology	Cat#3879S; RRID: AB_2255011
Mouse monoclonal anti-Tubulin (clone DM1A)	Sigma-Aldrich	Cat#T9026; RRID: AB_477593
Rabbit polyclonal anti-BMAL1	This paper	N/A
Bacterial and Virus Strains		
pAAV-hSyn-DIO-hM3D(Gq)-mCherry	Krashes et al., 2011	Addgene AAV5; 44361-AAV5
AAV5-EF1a-DIO-hChR2(H134R)-EYFP	Hope Center Viral Vectors Core	N/A
Cowpox virus Brighton Red	BEI Resources	NR-88
Zika-SMGC-1, GENBANK: KX266255	Isolated from patient (Wang et al., 2016)	N/A
Staphylococcus aureus	ATCC	ATCC 29213
Streptococcus pyogenes: M1 serotype strain: strain SF370; M1 GAS	ATCC	ATCC 700294
Biological Samples		
Healthy adult BA9 brain tissue	University of Maryland Brain & Tissue Bank; http://medschool.umaryland.edu/btbank/	Cat#UMB1455
Human hippocampal brain blocks	New York Brain Bank	http://nybb.hs.columbia.edu/
Patient-derived xenografts (PDX)	Children's Oncology Group Cell Culture and Xenograft Repository	http://cogcell.org/
Chemicals, Peptides, and Recombinant Proteins		
MK-2206 AKT inhibitor	Selleck Chemicals	S1078; CAS: 1032350-13-2
SB-505124	Sigma-Aldrich	S4696; CAS: 694433-59-5 (free base)
Picrotoxin	Sigma-Aldrich	P1675; CAS: 124-87-8
Human TGF-β	R&D	240-B; GenPept: P01137
Activated S6K1	Millipore	Cat#14-486
GST-BMAL1	Novus	Cat#H00000406-P01
Critical Commercial Assays		
EasyTag EXPRESS 35S Protein Labeling Kit	Perkin-Elmer	NEG772014MC
CaspaseGlo 3/7	Promega	G8090
TruSeq ChIP Sample Prep Kit	Illumina	IP-202-1012
Deposited Data		
Raw and analyzed data	This paper	GEO: GSE63473
B-RAF RBD (apo) structure	This paper	PDB: 5J17

REAGENT or RESOURCE	SOURCE	IDENTIFIER
Human reference genome NCBI build 37, GRCh37	Genome Reference Consortium	http://www.ncbi.nlm.nih.gov/projects/genome/assembly/grc/human/
Nanog STILT inference	This paper; Mendeley Data	http://dx.doi.org/10.17632/wx6s4mj7s8.2
Affinity-based mass spectrometry performed with 57 genes	This paper; and Mendeley Data	Table S8; http://dx.doi.org/10.17632/5hvpvspw82.1
Experimental Models: Cell Lines		
Hamster: CHO cells	ATCC	CRL-11268
D. melanogaster: Cell line S2: S2-DRSC	Laboratory of Norbert Perrimon	FlyBase: FBtc0000181
Human: Passage 40 H9 ES cells	MSKCC stem cell core facility	N/A
Human: HUES 8 hESC line (NIH approval number NIHhESC-09-0021)	HSCI iPS Core	hES Cell Line: HUES-8
Experimental Models: Organisms/Strains		
C. elegans: Strain BC4011: srl-1(s2500) II; dpy-18(e364) III; unc-46(e177)rol-3(s1040) V.	Caenorhabditis Genetics Center	WB Strain: BC4011; WormBase: WBVar00241916
D. melanogaster: RNAi of Sxl: y[1] sc[*] v[1]; P{TRiP.HMS00609}attP2	Bloomington Drosophila Stock Center	BDSC:34393; FlyBase: FBtp0064874
S. cerevisiae: Strain background: W303	ATCC	ATTC: 208353
Mouse: R6/2: B6CBA-Tg(HDexon1)62Gpb/3J	The Jackson Laboratory	JAX: 006494
Mouse: OXTRfl/fl: B6.129(SJL)-Oxtr$^{tm1.1Wsy}$/J	The Jackson Laboratory	RRID: IMSR_JAX:008471
Zebrafish: Tg(Shha:GFP)t10: t10Tg	Neumann and Nuesslein-Volhard, 2000	ZFIN: ZDB-GENO-060207-1
Arabidopsis: 35S::PIF4-YFP, BZR1-CFP	Wang et al., 2012	N/A
Arabidopsis: JYB1021.2: pS24(AT5G58010)::cS24:GFP(-G):NOS #1	NASC	NASC ID: N70450
Oligonucleotides		
siRNA targeting sequence: PIP5K I alpha #1: ACACAGUACUCAGUUGAUA	This paper	N/A
Primers for XX, see Table SX	This paper	N/A
Primer: GFP/YFP/CFP Forward: GCACGACTTCTTCAAGTCCGCCATGCC	This paper	N/A
Morpholino: MO-pax2a GGTCTGCTTTGCAGTGAATATCCAT	Gene Tools	ZFIN: ZDB-MRPHLNO-061106-5
ACTB (hs01060665_g1)	Life Technologies	Cat#4331182
RNA sequence: hnRNPA1_ligand: UAGGGACUUAGGGUUCUCUCUAGGGACUUAGGGUUCUCUCUAGGGA	This paper	N/A
Recombinant DNA		
pLVX-Tight-Puro (TetOn)	Clonetech	Cat#632162
Plasmid: GFP-Nito	This paper	N/A
cDNA GH111110	Drosophila Genomics Resource Center	DGRC:5666; FlyBase:FBcl0130415
AAV2/1-hsyn-GCaMP6- WPRE	Chen et al., 2013	N/A
Mouse raptor: pLKO mouse shRNA 1 raptor	Thoreen et al., 2009	Addgene Plasmid #21339
Software and Algorithms		

REAGENT or RESOURCE	SOURCE	IDENTIFIER
ImageJ	Schneider et al., 2012	https://imagej.nih.gov/ij/
Bowtie2	Langmead and Salzberg, 2012	http://bowtie-bio.sourceforge.net/bowtie2/index.shtml
Samtools	Li et al., 2009	http://samtools.sourceforge.net/
Weighted Maximal Information Component Analysis v0.9	Rau et al., 2013	https://github.com/ChristophRau/wMICA
ICS algorithm	This paper; Mendeley Data	http://dx.doi.org/10.17632/5hvpvspw82.1
Other		
Sequence data, analyses, and resources related to the ultra-deep sequencing of the AML31 tumor, relapse, and matched normal.	This paper	http://aml31.genome.wustl.edu
Resource website for the AML31 publication	This paper	https://github.com/chrisamiller/aml31SuppSite